University of Stavanger

Faculty of Science and Technology

MASTER'S THESIS

Study program/Specialization: Petroleum Geosciences Engineering	Spring, 2019 Open
Writer: Yvonne Nayive Jaimes Duarte	(Writer's signature)
Faculty supervisor: Nestor Cardozo External supervisor(s): Jan Tveiten, Schlumberger	
Title of thesis: Modeling of turbidite systems in deep-water, thrust-related bivergent anticlines.	
Credits (ECTS): 30	
Keywords: Trishear model Bivergent anticlines Forward modeling Unsteady flow Diffusion	Pages: 93 +enclosure: 0 Stavanger, June 15th, 2019

Modeling of turbidite systems in deep-water, thrust-related bivergent anticlines

by

Yvonne Nayive Jaimes Duarte

Master Thesis

Presented to the Faculty of Science and Technology

The University of Stavanger

The University of Stavanger

June 2019

Acknowledgements

This thesis was supervised by Nestor Cardozo, whom I want to thank for his valuable help during the entire thesis development. Especially his guiding with the explanations and use of the trishear model and his critical reading of the earlier versions of the manuscript.

I am also grateful with Jan Tveiten (Schlumberger) for guarantee the coupling between the trishear and GPM models and for his guidance during the process of learning the uses of the software.

A special thanks to my fellow classmate Hoang for his support at the initial stage of the thesis. And my dear family and friends, Isabel, Andrei and Alfred for being my support throughout my master studies.

Abstract

Modeling of turbidite systems in deep-water, thrust-related bivergent anticlines

Yvonne Nayive Jaimes Duarte

The University of Stavanger, 2019

Supervisor: Nestor Cardozo

In deep-water fold and thrust belts, thrust-related folds that switch vergence along strike can occur and are considered to have a major impact on reservoir distribution (Higgins et al., 2009). Syn-sedimentary processes resulting from the initiation and propagation of these structures modify the sediments distribution and deposition, as well as the channels pathways. In this thesis, forward modeling is applied to simulate seven cases related to two listric, oppositely verging thrusts that initially grow separately but with growth, they link. The model is implemented by coupling two independent but related models. A pseudo-3D trishear model, which simulates the kinematic growth of the thrust-related anticlines in terms of parameters such as fault slip, trishear angle, and fault propagation to slip ratio; and a forward stratigraphic model (GPM), which simulates geomorphological variations as result of sediment transport and erosion in a deep-water, turbidite setting.

The obtained models reveal that: a) the variation of the structure's center of curvature (Case 1 to 4) affects the confinement, migration and direction of the flow. After overpassing the structures the sediment distribution over the fan developed area can be i) a cone-shape fan elongated in the flow direction and ii) symmetrical cone-shape fan perpendicular to the strike of the structures; b) decreasing the TA and the P/S of one thrust with respect to the other

(Case 5 and 6) can block and deflect the flow. The blocking and posterior deflection favor the sediments transported by the unsteady flow to be accumulated as amalgamated sand-rich layers, which are deposited and trapped against the structure. However, diffusion results do not suggest preferential deposition of possible reservoir units adjacent to the anticlines; and, c) decreasing the timestep (Case 7), provide more time to the sediments to be mixed. It creates a more heterogenous reservoir (if existing) with a potential decrease in petrophysical properties. These results highlight the sensible response of sedimentation to active deformation since the flow pathway is continuously deflected, blocked or both.

Forward modeling techniques provide a better understanding of geological processes through time in order to perform predictive analysis of prospective sand-rich layers distribution. In addition, present an alternative exploration approach that can be applied in frontier zones where exploration data is limited.

Table of Contents

List of figures

List of Tables

1. Introduction

In deep-water fold and thrust belts, thrust-related folds that switch vergence along strike can occur (Higgins et al., 2009. Figure 1). Structures like these are present in, for example, the deep-water Niger Delta (Corredor et al., 2005). The development of such structures in potential hydrocarbon areas have significant exploration impact because they can influence: (i) the syn-sedimentary processes, which primarily depend on tectonic deformation (Covault and Graham, 2008), (ii) the development of thrust-related, wedge-top accommodation space in which turbiditic sediments can accumulate (Covault and Graham, 2008), and (iii) the distribution and connectivity of sand reservoirs in a stacked channel-levee system (Higgings et al., 2007).

Deep-water syn-kinematic sediments commonly serve as prolific hydrocarbon reservoirs, as well as they record relative sea-level fluctuations and tectonic episodes (Gordon, 2014). A recent interest on understanding the relationship between tectonic deformation and channel development (e.g., Owoyemi, 2004; Clark and Cartwright, 2009; Clark and Cartwright, 2012; Jolly, 2014, among others), and on the acquisition of 3D seismic data in active margins, has made possible to study the interaction of deep-water channels and seafloor structures (Jolly, 2014). Thanks to this, increasing understanding of how tectonic deformation influence sediment distribution in this setting has been possible (Clark and Cartwright, 2012). However, a better process-based understanding of how sedimentation responds to thrust deformation can help predict sediment distribution, channel pathways, reservoir geometries and improve the prediction of potential reservoir units.

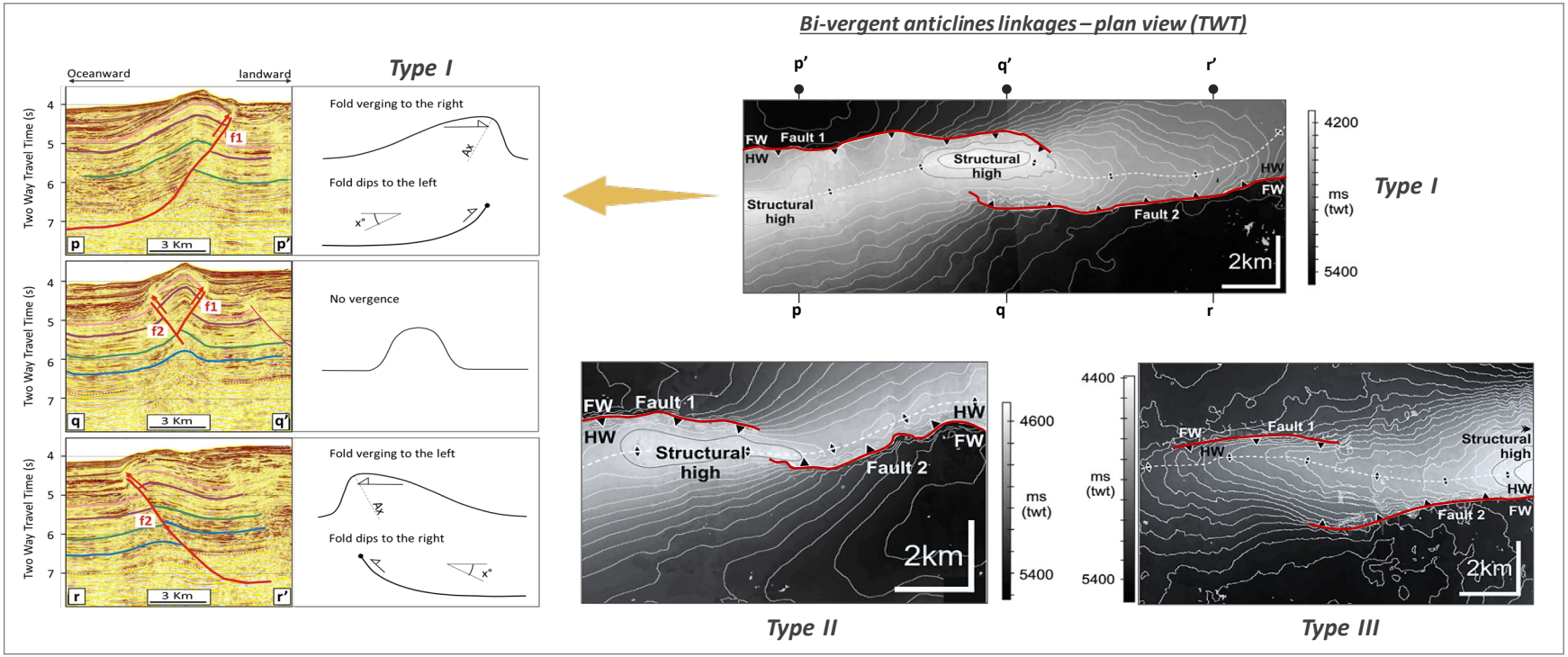

Figure 1. Niger Delta toe bi-vergent anticlines linkage types. (Right) Structural maps in two-way-time (ms) showing three types of linkage (Type I, II and III) associated with thrust-related folds that switch vergence along strike. Although the three types change vergence along strike, the deformation on the transfer zones varies with depth because is dependent on how the thrusts overlap (Higgings et al., 2007). (Left) Seismic lines showing a thrust-related anticline switching vergence along strike in a type I linkage. Seismic sections are in two-way-time (ms) and their locations are shown on the type I map (right). Modified from Higgings et al. 2007.

1.1 Aims of the study

The aim of this thesis is to study the evolution of syn-depositional turbidites in deep-water fold-and-thrust belts, and specifically above thrust-related anticlines that switch vergence along strike. To achieve this goal, I integrate forward modeling simulations of (i) tectonics, using a kinematic trishear model in three-dimensions (based on Cardozo and Brandenburg, 2014), and (ii) ground process modelling (GPM), which simulate the geometry and lithology of stratigraphic sequences as a consequence of sea-level change, tectonic uplift or subsidence, variation in sediment input, and transport rates. For GPM, I use the Petrel plugin GPM (Tetzlaff et al., 2014).

1.1.1 Specific objectives

The following specific objectives illustrate the main strategy used in order to understand the evolution of syn-depositional turbidites in deep-water, thrust-related, bi-vergent anticlines:

- Simulate the factors controlling turbidites related to bi-vergent anticlines above listric thrusts, by testing variations in thrust-fold kinematics, sediment transport, deposition, and erosion.
- Understand the spatiotemporal variations in the morphology and geometry of the sediments when the main controlling distribution parameters are tectonically related.
- Discuss how the interactions between a growing fold and syn-deposition can favor the presence of potential reservoir units.

2. Research methods

2.1 Trishear modeling

Although useful to fill the unknown space, kink-band migration models that result in similar fold geometries, uniform dips, and parallel limbs, such as fault-bend fold, fault-propagation fold, and detachment folding (Figure 2 a-c) (Pei et al., 2014), provide limited insight about the mechanisms that take place in thrust-related folds (Kameda, 2000). These structures often show non-similar geometries and thickness variations in the fold limbs (Figure 2d). Variations of fold geometry are highly dependent on the units' thickness, sediment composition, and mechanical stratigraphy involved in the deformation (Mitra, 2002).

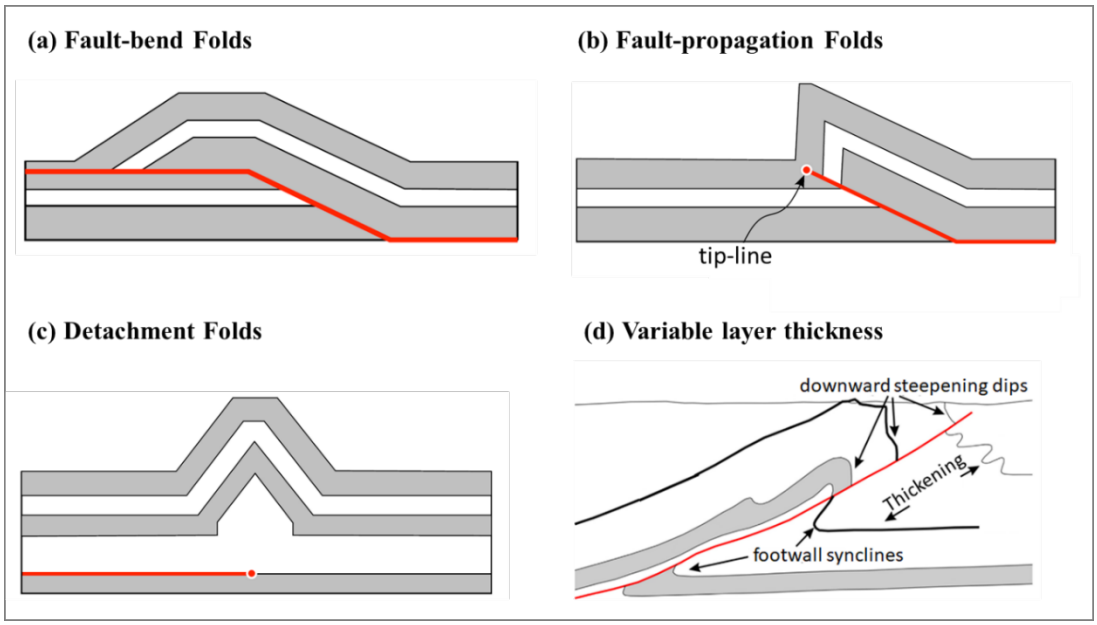

Figure 2. Kink type fault-bend fold and fault-propagation fold models (a, b) (Suppe, 1983; Medwedeff and Suppe, 1997), detachment fold (c), and layer geometry and thickness variability in a natural example of a thrust-propagation fold (d) (Allmendinger, 1998). Modified from Pei et al. (2014).

Erslev (1991) and Allmendinger (1998) propose a kinematic model of fault-propagation folding in which the decrease in displacement along the fault is accommodated by

heterogeneous shear in a triangular zone radiating from the fault tip (Figure 3) (Hardy and Allmendinger, 2011). This model is called trishear, and in two-dimensions it results from the combination of six parameters that are linked to the fault geometry and its propagation history: (i) fault-tip location (x and y), (ii) fault dip (ramp angle), (iii) fault propagation to fault slip ratio (P/S), (iv) apical angle of the triangular zone or trishear angle (TA), and (v) fault slip. In three-dimensions, a simple linear variation of P/S, TA, and fault slip along the fault tip line increases the number of model parameters to fourteen (Cardozo, 2008). A disadvantage of trishear is the uncertainty in determining which parameter combination influences the most natural folding structures in two-dimensions and three-dimensions (Pei et al., 2014). However, trishear inverse modeling allows fitting models to natural structures and their associated uncertainties (Cardozo and Aanonsen, 2009; Cardozo et al., 2011). The results not only help to identify the range of possible best-fit models, but also reconstruct the possible evolution of the fault-related fold (Hsieh et al., 2012).

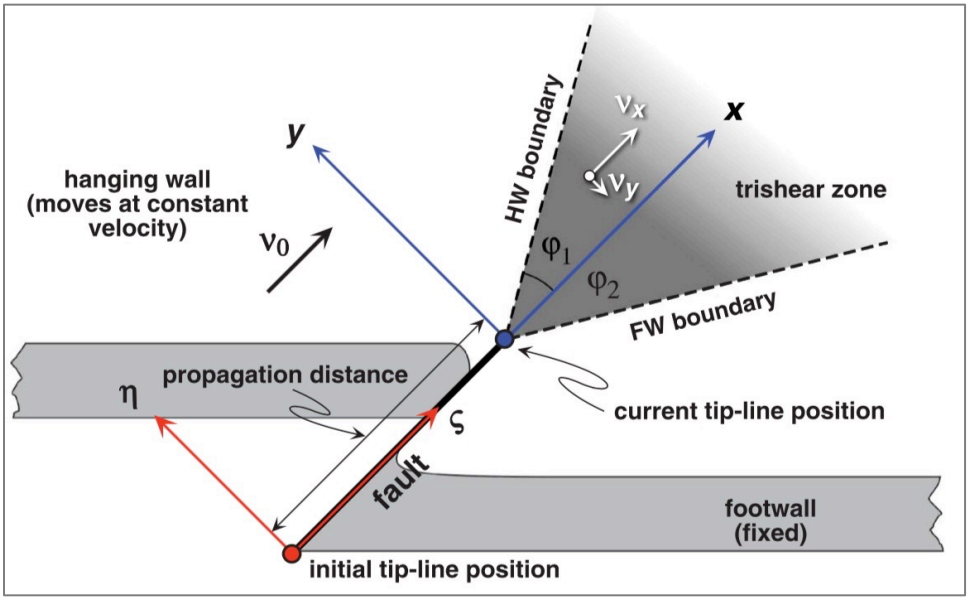

Figure 3. Sketch illustrating the main elements of the kinematic trishear model. Based on Hardy and Allmendinger (2011).

Cardozo and Brandenburg (2014) used a kinematic trishear approach to simulate folds above listric thrusts propagating from a detachment level. The model is based on: (i) a circular thrust geometry defined by a center and radius of curvature, (ii) a maximum central angle beyond which the thrust is planar, (iii) inclined shear above the circular thrust, and (iv) trishear in front of the thrust (Figure 4). The model can be run forwards and backwards, such that one can search within a parameter space of defined ranges, the parameter combination that best restores the deformed beds to their initial geometry (Cardozo and Brandenburg, 2014).

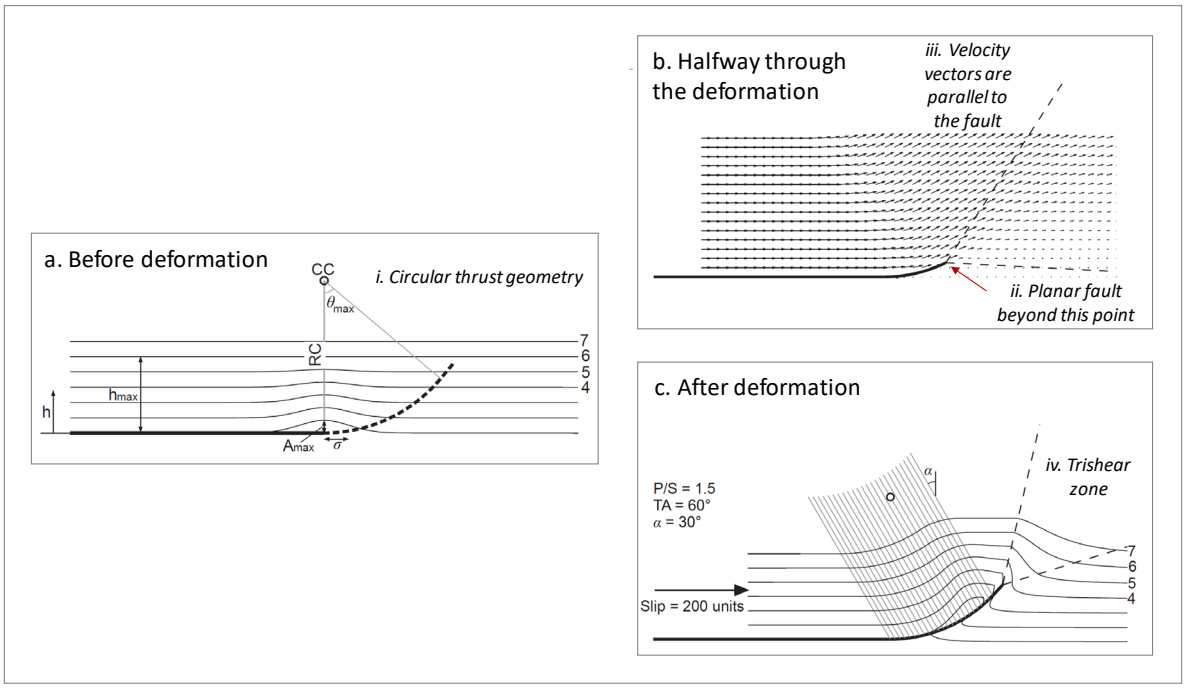

Figure 4. Kinematic trishear model for folds above listric thrusts. (a) Geometry, (b) velocity field, and (c) Final geometry. From Cardozo and Brandenburg (2014). A pseudo-3D implementation based on this 2D model was used in this thesis.

For this thesis, a Matlab (Mathworks) pseudo-3D extension of the model proposed by Cardozo and Brandenburg (2014) was used. In essence, this pseudo-3D implementation consists of serial cross sections parallel to the thrust slip direction. In each one of these sections, the 2D solution of Cardozo and Brandenburg (2014) is used. This pseudo-3D

implementation allows modelling thrust-related anticlines dying along strike (i.e. decreasing fault slip along strike), and interacting anticlines with opposite vergence, which is the case we are interested in.

2.2 Stratigraphic forward modeling

Stratigraphic forward modeling is based on simulating dynamic sedimentary processes involving sediment transport, erosion and deposition. In order to reproduce a realistic three-dimensional model suitable to predict sediment distribution, the simulation process considers variable paleogeographic conditions (e.g. sea level changes, amount and type of sediment source input, and tectonic events) (Christ et al., 2016). I use in this thesis a simulator for stratigraphic and sedimentary processes called Geological Process Modeling (GPM, Schlumberger) which works as a plugin for the software Petrel (Schlumberger). This is a simple, yet realistic, large-scale, and long-term sedimentation model used to estimate paleographic conditions. It is also useful for testing several input parameter combinations with the objective of best fitting present seismic, well logs, and outcrop data (Tetzlaff, 2007). Because the model is deterministic (but not the input parameters, which can be stochastic), the geological system state is obtained by propagating sampled initial parameters or conditions forward (Skauvold and Eidsvik, 2018). In general, the model combines five parameters as primarily input (i) sediment components and their properties, (ii) basin configuration through time, (iii) sources, sinks and boundary conditions, (iv) sea-level curve and, (v) modeling time interval (Tetzlaff et al., 2014).

Boundary conditions such as sediment transport, erosion and deposition need to be set before the start of the stratigraphic simulation process. These physical processes can be modeled by three methods (i) diffusion, (ii) steady flow, and (iii) unsteady flow.

Diffusion is the simplest physical process, and it assumes that the sediments move downslope in agreement with the slope gradient. In other words, topographic highs will be eroded, and the sediments eroded will be deposited in basins (Kyrkhebø, et al., 2000). Diffusion assumes the finer sediments will be deposited farther and the coarser sediments closer to the source (Tetzlaff et al., 2014). Diffusion is used to model secondary transport mechanisms (small-scale) and is usually combined with free surface flow methods (e.g. steady flow, unsteady flow) (Tetzlaff, 2007). The small-scale functionality of diffusion is a disadvantage, because it does not consider that collapsing slopes can contribute to reworking of sediments and mixed sediment grain size. But, despite being a secondary process, features such as channels, canyons, etc., will have a sharp and unrealistic shape without diffusion (Tetzlaff, 2007).

GPM simulates free-surface flow, "*an interface between a liquid and a second medium that is unable to support an applied pressure gradient or shear stress*" (Abdou, 2001), for steady flow (river flow) and unsteady flow (turbidity currents and river floods) (Tetzlaff et al., 2014). The model assumes that the horizontal component of the vertical velocity profile does not vary anywhere. In consequence, the model just considers the vertically averaged horizontal velocity vectors (Tetzlaff, 2007). The main disadvantage is that the method does not account for changes in the flow direction (e.g. helical flow in river turns and vertical eddies). It accounts only for changes in the magnitude of flow velocity with depth and records these changes at every point (Tetzlaff, 2007 and Tetzlaff et al., 2014). Nevertheless, this simple representation of free-surface flow makes possible to simulate geologic time scale models (Tetzlaff, 2007). Additionally, GPM assumes the flow acceleration is governed by (i) the gravity and the elevation of the water surface, (ii) the viscosity of the fluid, (iii) the friction of the fluid against the bottom, and (iv) the acceleration due to external forces, such as wave action (Tetzlaff, 2007).

In general, both steady and unsteady flow will erode, transport and deposit sediments primarily considering the grain sizes, the velocity of the flow, and depth (Tetzlaff et al., 2014). Steady flow is used when the flow velocity and depth are undisturbed through time. A flow can be considered as steady if after several hours it continues undisturbed. While unsteady flow is used to simulate unstable flow velocity and depth through time. A flow can be considered as unsteady when it runs over a determined amount of time and when the flow velocity and depth vary in a short lapse of time (Tetzlaff et al., 2014).

To help with the theoretical approach to forward-modeling syn-kinematic turbidites, the process-based model-elements required by the software are linked and changed in agreement with a pre-established time interval that display sequence boundaries depending on the number of cycles set. The most important GPM elements that will be discussed later in detail are: eustatic sea-level changes (user-defined), diffusion coefficient, erodibility and transport coefficient (user-defined - represent the magnitude of the erosion and how easily the sediment can be transported), sediment lithology, grain size, and flow velocity (user-defined size of the water source). Since the goal of this thesis is to understand the factors controlling turbidites related to bi-vergent anticlines above listric thrusts, the GPM processes considered here are diffusion and unsteady flow. By the end of the modeling, it is expected that the resulting model shows a coherent and realistic stratigraphy controlled by the input variables and the boundary conditions at the previously established geological time (Skauvold and Eidsvik, 2018).

2.3 Implementation

As explained in section 2.1, tectonic deformation, the growth of a thrust-related, bi-vergent anticline is simulated using a pseudo-3D trishear model for fold(s) above listric thrust(s).

Sediment deposition and erosion due to turbidite currents is simulated using GPM. Thus, the two models, tectonic (trishear) and sedimentation (GPM), must be integrated. This is accomplished as described in Figure 5.

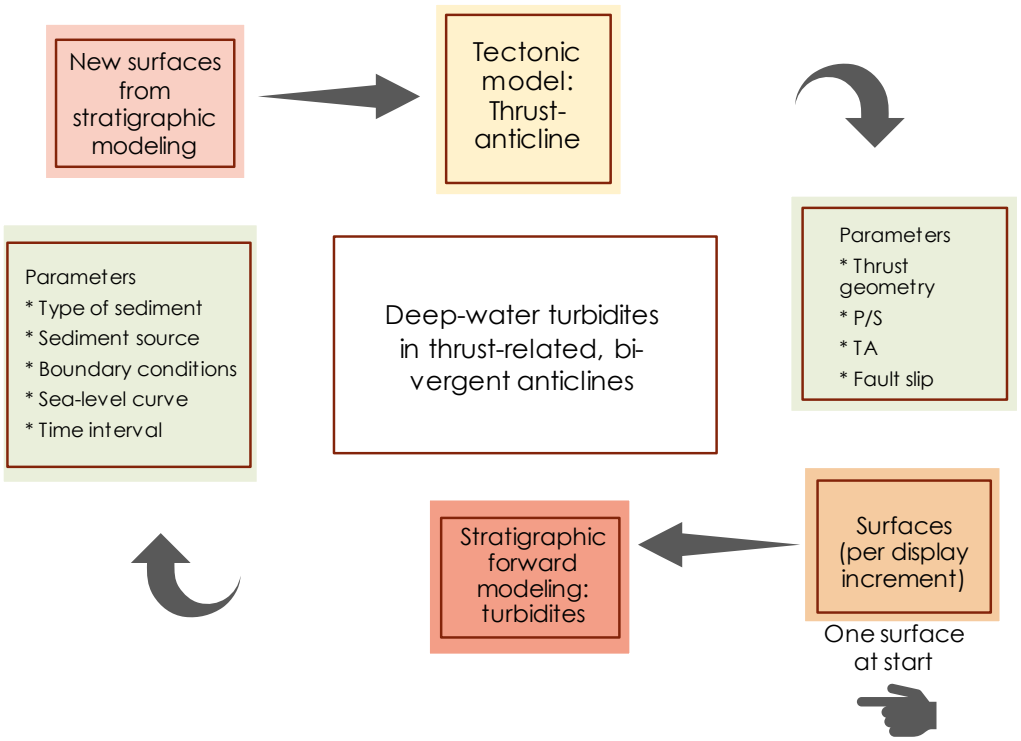

Figure 5. Workflow showing the required steps necessary to integrate tectonic deformation (trishear) and sedimentation (GPM), including the parameters involved in each model. Based on Malde (2017).

The starting point is a GPM model with a gently dipping surface below sea level. This model is run for a determined display increment in GPM and then it is imported into the trishear model in Matlab. Then, in Matlab, the surfaces from the GPM model are deformed according to the pseudo-3D trishear model. These deformed surfaces are then sent back to GPM, for another step of sediment erosion and deposition, and then again into Matlab for tectonic deformation. This cycle is repeated for several display increments until the desired total thrust slip and anticline growth is accomplished.

3. Model Building

In this chapter, the coupling of the tectonic (trishear) and sedimentation (GPM) models described in section 2.3, is implemented. The main purpose is to optimize the parameters that control mainly the sedimentation model. Hence, many realizations are run in order to find out the best parameter combination GPM needs to simulate syn-sedimentary turbidites deposition (based on analogs). In general, these parameters are tested by propagating ideal initial conditions forward in time and applying different ranges of sea-level, sediment supply, sediment erosion, and flow.

The goal is to determine if it is possible to reproduce the influence that the actively growing thrust-related anticlines have on the seabed channel response and the sediment distribution on submarines fans, taking into account what is already known for such settings as in the Niger Delta (Deptuck et al., 2003; Adeogba et al., 2005; Heinio and Davies, 2007, Clark, 2013, Jolly, 2014), the Gulf of Mexico (Posamentier, 2003), the Nile Delta (Clark and Cartwright, 2012, Clark, 2013), Brunei (Demyttenaere et al., 2000) and offshore West Africa (Gee and Gawthorpe, 2006). Channels in tectonically active deep-water settings undergo changes in sinuosity and direction. Channel sinuosity changes are considered critical for reservoir prediction because a decrease in sinuosity increases the channel incision, decreasing the levee development and vice-versa (Clark and Cartwright, 2012). Increase in channel incision is associated with major sediment erosion or non-deposition and lack of lateral channel migration (Clark and Cartwright, 2012). Lateral channel migration produces lateral amalgamation of individual channels that could result in a more prolific reservoir. In general, channel-levee relationships are important because they are qualitative indicators of how sediments respond to deformation and provide detail information about sand deposition. On

the other hand, changes in channel direction due to active seafloor perturbations indicate that the original channel flow path was deflected or blocked (Clark and Cartwright, 2012). Deflection of the flow path occurs when the original channel location is shifted due to a growing structure (Figure 6). Shifting of the flow path remains active if the uplifting structure is active (Clark and Cartwright, 2012). Deflection produces lateral amalgamation of channels and a more prospective reservoir.

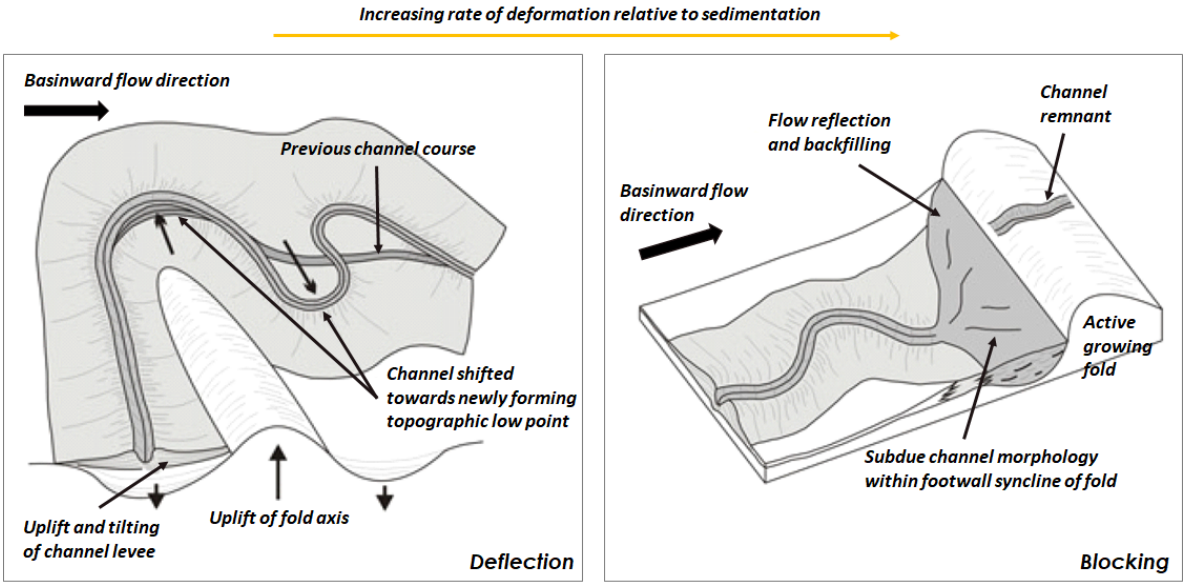

Figure 6. Channel flow path responses to a growing structure. Left: Deflection, right: Blocking (Clark & Cartwright, 2012).

Blocking of the channel occur when the uplift rate exceeds the sedimentation rate (Figure 6). Blocking of the channel produces segmentation of the original channel (Clark and Cartwright, 2009). One part remains downstream of the blocking structure, while the other part that remains upstream is softened and filled, although it is probably preserved (Clark and Cartwright, 2009). As with deflection, blocking has implications on reservoir development since the blocking structure controls the thickness and lateral extension of the channel upstream and downstream. Downstream the channel will have a sand-rich lateral migration,

while upstream the channel will have a thickness reduction and it will be isolated (Clark and Cartwright, 2009).

Prior knowledge about the channel flow path behavior helps visualizing the expected result after the simulation and what would be considered a correct and coherent model for turbidite deposition above compressional structures. Since GPM is a basin-scale software, it simulates regional geological processes that provide a big-scale idea about sediment distribution and channel path changes (Acevedo et al., 2014). Nevertheless, it is not possible to simulate a reservoir-scale model where detail geometrical relationships related to the active structures (e.g. onlap, downlap, progressive rotation, among others, Figure 7) can be recognized (Acevedo et al., 2014, Clark and Cartwright, 2011). Therefore, the models of this thesis mainly focus on understanding and recognizing the changes in the flow path described above and how these changes influence sediment distribution.

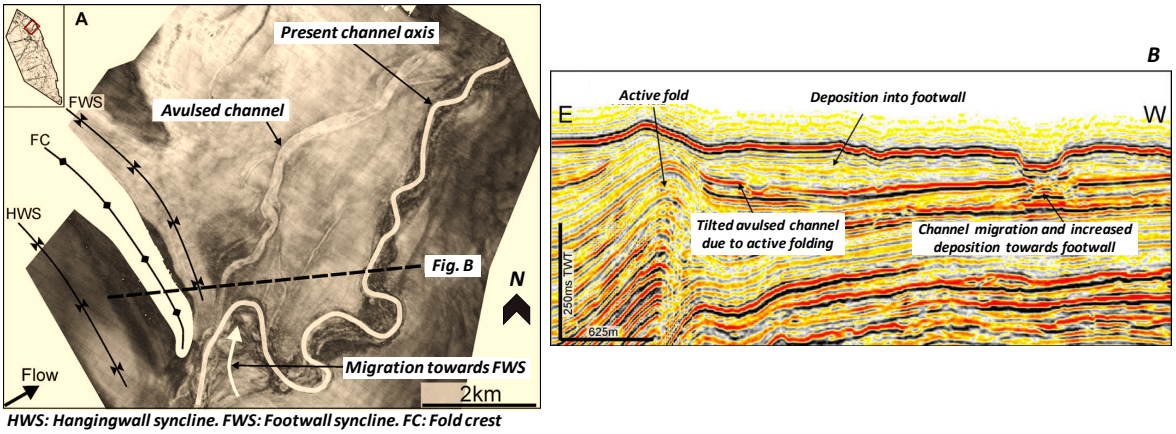

Figure 7. Right. Channel flow path diverted by the growth of the structure. Left: Seismic line showing the increase in the seismic reflector tilting due to the structure grow (Clark & Cartwright, 2012).

3.1 Model setup

As mentioned in section 2.2, the model requires an initial surface that represents the initial basin configuration. In this thesis, the basin-floor surface that serves as an initial surface for the simulations is a gentle surface (maximum 2 degrees dip. Regional slopes associated with deepwater settings, such as in the Niger Delta, range between 1.5 and 2 degrees) below sea level. The initial surface dip is towards the east. For the unsteady flow process, the area is sourced from a feeder channel by defining a "source position" in the southwest or the west-southwest (Figure 8).

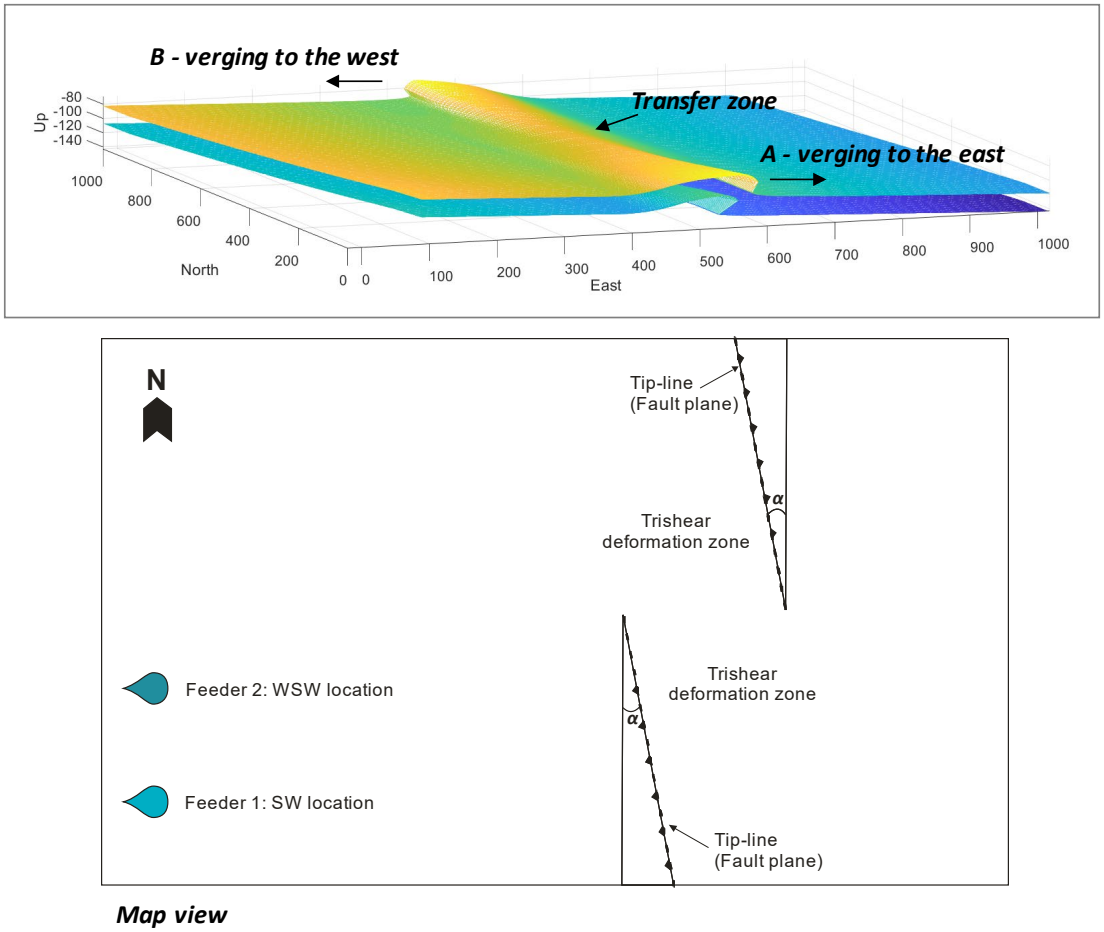

Figure 8. Map view of the general situation to be modeled. The fault planes and the two different flow source (feeder) locations used during the simulations are indicated.

Several time cycles were used in order to test the development of the structure but in general, the time cycle that works better is 100 ky. The display interval of the models is 10 ky such that the models have 10 timesteps. The surface dimensions and the grid cells resolution are variable and depend on the detail required for the simulation.

This project is organized in accordance with the relations between the different cases that will be modeled. The main purpose is to keep track of what settings are applied during each simulation and to avoid the repetitive selection of constant parameters. The cases are grouped or can be discriminated from each other mainly by the variations in the trishear model parameters (geometry changes). This thesis explores mainly 7 cases. The first four cases show variations in the center of curvature of the thrusts, and width and location of the transfer zone between them. In the fifth case, the propagation to fault slip ratio (P/S) of the east-vergent thrust is varied, and for the sixth case, the sea-level is raised and the apical angle of the triangular zone or trishear angle (TA) is different in both thrusts. In the seventh case, the timesteps are decreased from 10 to 2 ky, and 50 timesteps are made in order to make a more detailed analysis of sediment distribution.

3.2 Key Model Parameters

Before performing the simulations, it is important to understand the interaction between tectonic deformation and turbidites deposition. For this, it is necessary to fine-tune the model parameters by systematically changing them. The purpose is to produce results that are similar to analogue areas (e.g. the Niger delta toe thrust).

For the initial models, the only fixed parameters that define the initial setup of the model are the initial basin geometry and the time interval (section 3.1). The most critical parameters are eustatic sea-level, diffusion coefficient, erodibility, transport coefficient, sediment setting

(lithology, grain size, contribution), and flow velocity. Remaining parameters, such as porosity, density, amount of tectonic subsidence among others, have no effect in the scenarios simulated here but they affect more complex scenarios that are beyond the scope of the thesis.

3.2.1 Eustasy

For the purpose of the thesis, the sea-level curve is included as an input. Although a sea-level curve is not strictly required by GPM and, if not provided, it is assumed to be at elevation zero (Schlumberger, 2016), it is important to explore if the variations in sediment-flux rates related to changes in eustatic sea-level affect drastically the deep-water sediment distribution patterns. GPM uses as default two global sea-level curves: The Haq and the Exxon global sea-level curves. These curves predict sea-level variations through time from a globally averaged coastal onlap chart (Carter, 1996). GPM accepts refined or adjusted curves to account for local sea-level changes. For the initial simulations, the short-term curve of Haq et al. (1987) was chosen. For later simulations and to understand the impact of sea-level changes on sediment deposition, the global sea-level curve is increased and stays at a constant elevation. However, local sea-depth variations through time due to erosion and deposition are expected (Schlumberger, 2016).

3.2.2 Sediment input

Four different lithologies are modeled: coarse sand, fine sand, silt, and clay. GPM models each lithology and assigns to them a distinctive color depending on the composition (Schlumberger, 2016). The color is a single color if the lithology is not mixed, e.g. coarse sand (red), fine sand (green), silt (blue) and clay (black), but if the sediments comprise mixed lithologies they are represented as additive color mixtures (Schlumberger, 2016). To test the

preferential sediment distribution and their relationship with the growing structure, the sediments grain properties (size, density and fraction) are varied. This is because turbidity currents don't just carry on fine sediments in suspension, but rather they are the most important mechanism for transport coarse-grained sediments towards deep-marine settings by fluid turbulence (Reading and Richards, 1994). In the Niger Delta for example, the main source of sediment supply can transport sediments with a grain size up to coarse-grained sand and gravel in a variable range of concentrations during flood events (Jolly, 2014). During sea-level fall periods, different sediments sizes will reach deep-water environments. The following parameters (Table 1) were tested and adjusted until the results show the grain property distribution and diameter that best fit an environment rich in sand size fractions in agreement with a major petroleum-bearing unit such as the Agbada formation in the Niger delta (Jolly, 2014).

Table 1. Grain properties

Lithology	Grain Properties		
	Diameter (mm)	Density (g/cm^3)	Fraction ranges
Coarse Sand	1.2	2.7	0.38 - 0.42
Fine Sand	0.5	2.65	0.38 - 0.39
Silt	0.02	2.6	0.12 - 0.14
Clay	0.02	2.55	0.07 - 1.0

Therefore, the sediment contribution was assumed to be mostly sand and in minor proportion silt and clay. The sediment fractions were varied to show the preferential distribution of the sediments. This is discussed in detail in the results section.

3.2.3 Diffusion coefficient, erodibility and transport coefficient

The model requires a diffusion coefficient and a diffusion curve that is used to simulate the amount of erosion. The strength of the erosion is controlled by the diffusion coefficient

(m^2/a). The diffusion curve acts as a unitless multiplier (Schlumberger, 2017); this curve shows a slow and progressive increase at relatively shallow water and above sea level, where the sediments are more exposed to wave action and aerial erosion, whereas the diffusion values decrease below sea level. In addition, GPM considers that the diffusion coefficient is not equal everywhere and each sediment diffuses at a different rate. In general, GPM diffusion is depth, sediment type, and grain size dependent (Tetzlaff, 2007). Since the initial surface is located below sea level where the erosion is less strong, the diffusion values were kept below 10 m^2/a.

Erodibility controls how easily erosion will occur and how much materials through time will be removed and deposited in the basins (Schlumberger, 2017). The transport coefficient on the other hand enables to simulate how efficient the sediments can be transported. These two coefficients are environment dependent (Kyrkhebø, et al., 2000).

Erodibility values are kept between 50 and 70 % because for these values, the structure does not experience a dramatic erosion effect. Several values were tested for the transport coefficient and values between 0.18 and 0.22 were chosen since they make the transportability reasonable when combined with the flow velocity for unsteady flow.

3.2.4 Flow velocity

This parameter is the most sensitive. It is linked to the diffusion and unsteady flow geological processes. It is considered the principal mechanism for transporting sediments in GPM (Tetzlaff, 2007), and it is used to calculate the transport capacity which is dependent on the flow depth and velocity (Schlumberger, 2016). This parameter combines mainly two inputs, (i) a water supply curve, and (ii) a source position map. The water supply curve controls water velocity through time (Schlumberger, 2016). Additionally, the water supply curve is

combined with the fluid element depth that controls the number of particles added in the flow and a delta time element that is the internal computational time step that allows the particles in the flow to settle down (Schlumberger, 2016). The source position map controls the water and sediment flow rates (Schlumberger, 2016). Since the source is cell size dependent and very sensitive to perturbations in the model surface, trial and error is needed for the calibration of the flow velocity (Schlumberger, 2016). For that reason, the unsteady flow process without diffusion was tested several times with the purpose of calibrating first the flow velocity and avoiding anomalously and unrealistic large flows. In addition,, the location of the source position map was varied in order to represent variations in sediment distribution. This is discussed in detail in the results section.

3.3 Initial (test) simulations

In the initial simulations, the parameters that best fit the desired results described in section 3 are searched. The objective is to find the best range of parameter values in a low-resolution model, thus saving computation time. These parameter values are then tried later in higher resolution models.

To demonstrate how both models, trishear and GPM, work in practice, three tests cases over a 100 ky time cycle were run. The first and second case involve testing the initial surface elevation and sediment diffusion. The third case involves testing the unsteady flow using the best initial surface elevation from the first two cases (Figure 9).

The first case was created with the purpose of recognizing the most appropriate initial surface elevation and determining how this initial elevation is affected by sediment diffusion over a 100 ky time cycle. 30 models were run to estimate the best diffusion results. For this case, I

used a grid consisting of 41 cells in X and 21 cells in Y, each cell of size 50 x 50 m. The region modeled consist of a rectangle 2 km long and 1 km wide.

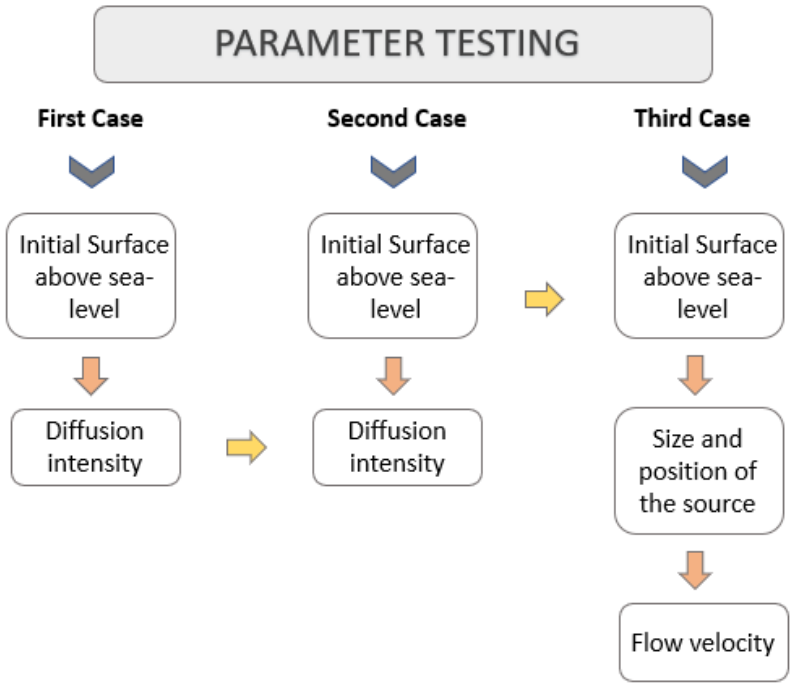

Figure 9. Initial (test) simulations for parameter testing

The basin-floor surface or initial surface is a gentle surface (max 2 degrees dip) dipping toward the east. The initial surface was fixed 15 m above sea-level in its shallower part (Figure 10, left). The objective was to input to the basin sediments coming for the area above sea level, and test the diffusion intensity with different diffusion coefficient values ranging from 0.07 to 0.8 m^2/a. In a first stage, the diffusion curve was maintained as the software default (values increasing slightly and almost linearly above sea level; Figure 10, right) but the diffusion coefficient values were varied gradually between the chosen range. Because diffusion is a time-dependent smoothing process, the range of values chosen was maintained relatively low to avoid the surface destruction, as mentioned in section 3.2.3.

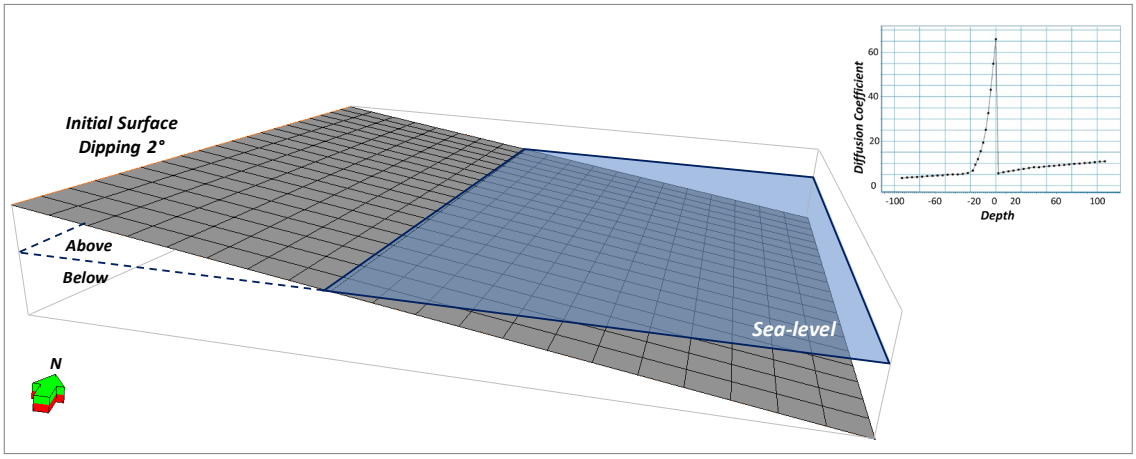

Figure 10. Initial surface configuration (left) and default diffusion coefficient curve (right). Arrow points north.

Over time and because of the slope of the initial surface, the sediments were diffused downhill towards the east (basin location). Depending on the simulated diffusion intensity, the amount of sediments deposited, and their thickness vary. When diffusion coefficient values are greater than 0.1 m^2/a, an abnormal thick wedge develops after the first-time cycle (the area above sea level is totally eroded and deposited in the basin). Contrary, values less than 0.1 m^2/a create a more realistic distribution of the sediments (Figure 11 A and B). The next stage was to adjust the diffusion curve values in such a way that over time when the structure starts to grow, the sediments accumulated on both sides of the anticline do not show drastic thickness variations but diffuse enough to show sediment variations.

As mentioned in section 3.2.3, the diffusion process in GPM involves a diffusion coefficient and a diffusion curve (unitless multiplier). Both diffusion parameters after been multiplied result in the total diffusion coefficient to be applied in the model. Hence the importance to test the model with both. In general, high diffusion curve and coefficient values would give as a result high total diffusion coefficient values that would produce an abnormal increase in the erosion rates. For this set of simulations and because part of the initial surface is located above sea level, when the curve coefficient values were higher than 10 (unitless), the

simulations showed an increase in the eroded and deposited sediments, especially in the initial time-cycles, where more sediments are available (Figure 11A). On the other hand, when diffusion curve values were maintained below 10 (unitless), the erosion rates and the sediments deposited decreased showing a more realistic thickness (Figure 11B).

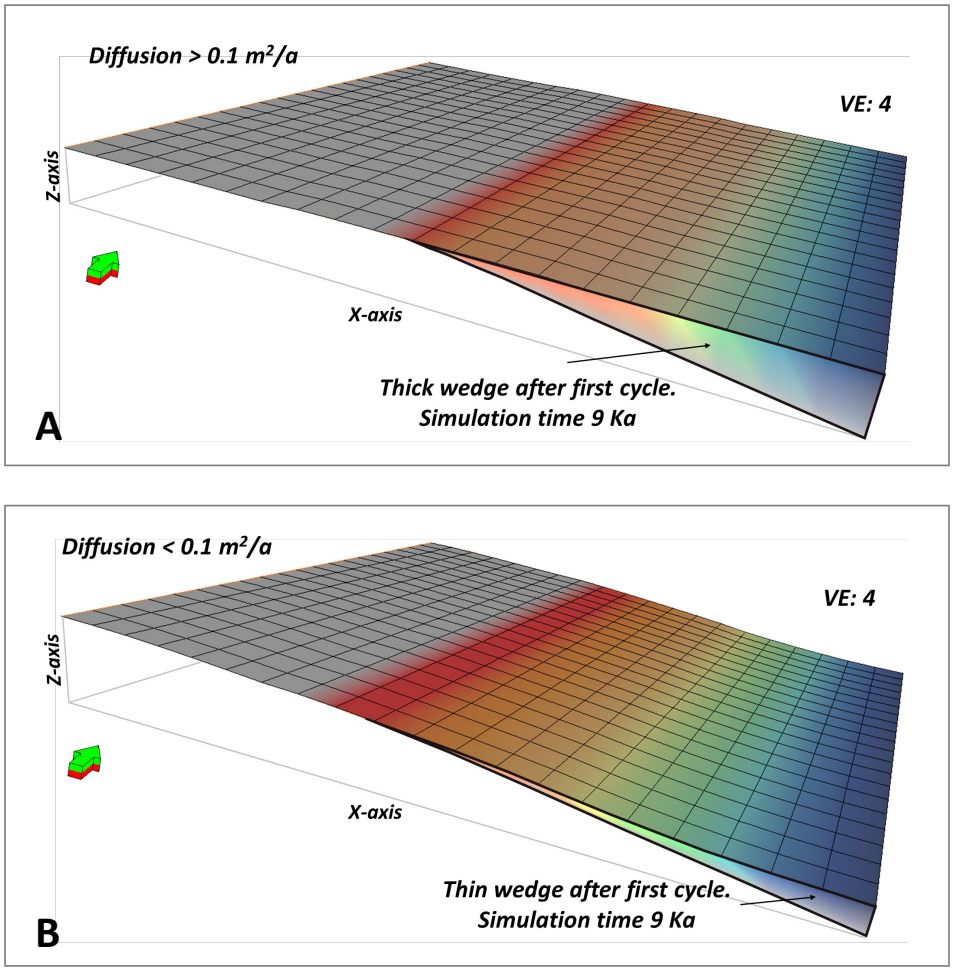

Figure 11. Sediments deposited after the first-time cycle (9 ka). A. Diffusion >0.1 m^2/a. B. Diffusion <0.1 m^2/a. Green arrows points north. The colors are associated with the modeled lithologies, Coarse sand (red), fine sand (green), silt (blue) and clay (black).

The second case was created with the purpose of testing the diffusion curve and diffusion coefficient ranges obtained in the first case, with an initial surface elevation below sea level over a 100 ky time cycle. 10 models were run to test different elevations below sea level. As

in the first case, the grid consists of the same number of cells and same cell size, and the region modeled has the same size. The basin-floor surface or initial surface is a gentle surface (max 2 degrees dip) dipping toward the east.

In the second case, the initial sloping surface was fixed at elevations 20 m and 40 m below sea-level in its shallower part. Since sediment diffusion is less strong below sea level, diffusion curve values below 10 (unitless) and diffusion coefficient values less than 0.1 m^2/a give coherent and realistic sediment thickness results. The main difference in these set of models is that, when a deeper surface is used (-20 m and -40 m), the thickness variations on both sides of the structure is less dramatic (Figure 12) because diffusion has a lower impact on surfaces below sea-level. In general, when compared, the tested surfaces below sea level (-20 m and -40 m) do not show large thickness changes and both can be used in the simulations.

The third case was created with the purpose of simulating the unsteady flow process (diffusion was not considered here). This case aims to find the best position and size for the unsteady flow source, the flow velocity and the transport coefficient over a 100 ky time cycle. 40 models were run to find the best parameters. The number of cells, resolution, and size of the modelled domain are the same than in the first two cases. The basin-floor surface or initial surface (for this test) was located 40 m below sea-level (in its shallower part) and has a gentle surface (max 2 degrees dip) dipping toward the east. The chosen elevation below sea level of the initial surface was based on the results obtained from the second case.

The third case can be considered as the most sensitive because searching for an appropriate flow velocity parameters range involves several calibrations. As mentioned in section 3.2.4, the flow velocity must be verified first, before allowing sediment erosion and transport to occur. Because the source depends on the position, the number of cells, the grid resolution

and the water supply curve (which controls water velocity through time), multiple simulations were performed to decide the best location and the best size of the source that gives an appropriate amount of water and water velocity, and which prevents the flow to pass over the structure.

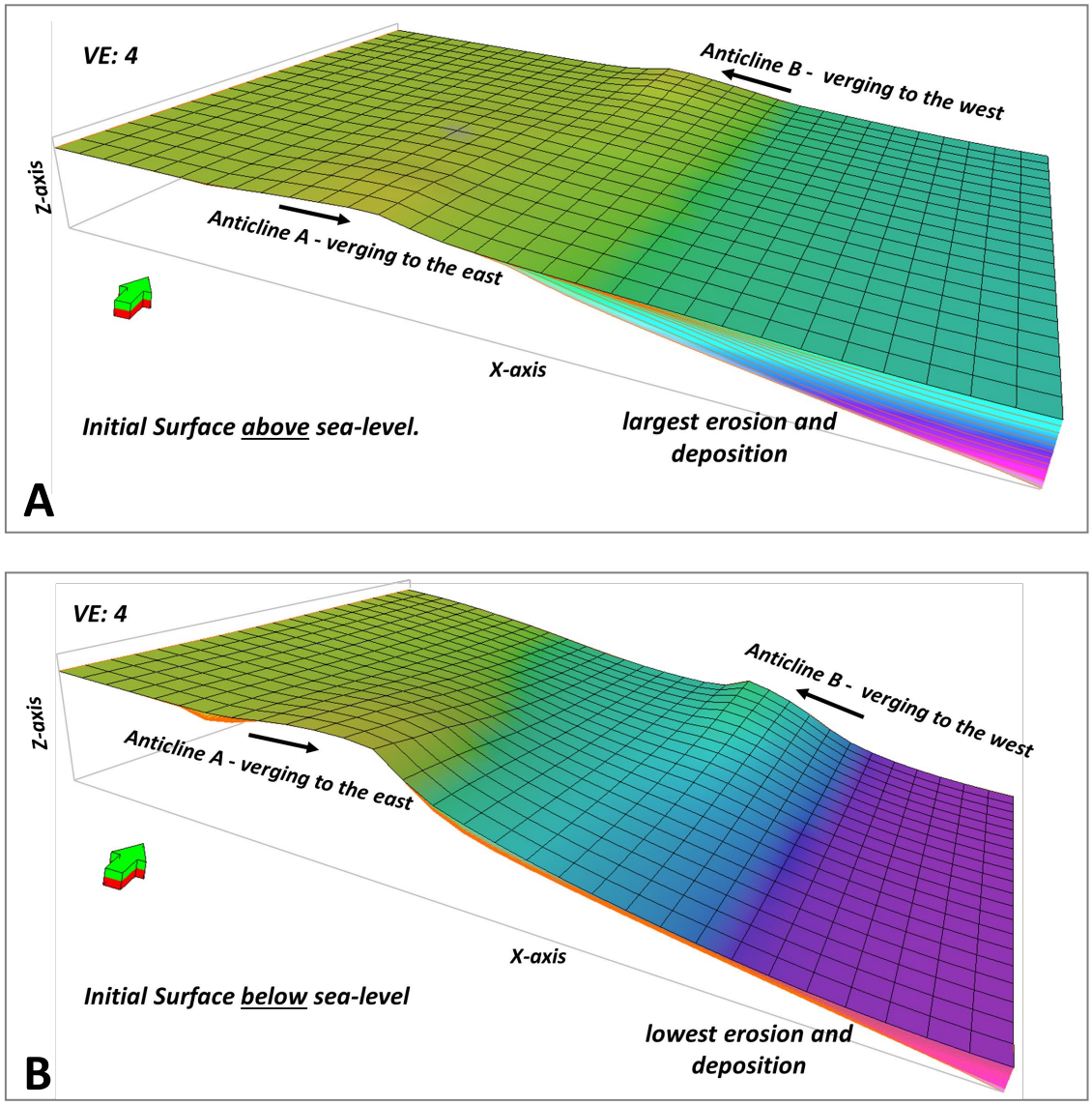

Figure 12. Sediment deposition comparison when an initial surface below and above sea -level are used. The colors mean depositional depth varying from shallow (green) to deep (purple). Green arrows point north.

First, the source position was fixed at the northwest corner of the model. The source initially covered approximately seven (7) cells of 50 x 50 m, and a water supply curve through time with values below 0.4 m/s. The results of this simulation show that the flow direction is affected by the model boundaries. Since the flow process is gravity based, the growth of the structure deviates the flow out of the model area. Also, the remaining flow passes over the anticline instead of being diverted by it (Figure 13A). This indicates that the flow rate is too high.

Then, the parameters were maintained as before, but the source position was changed from the northwest to the southwest (Figure 13B). The resulting flow shows no influence by the model boundaries. To the contrary, the flow is modified by the growing structure. However, the flow is still not been diverted correctly and it crosses the structure (Figure 13B).

Because the flow is now not influenced by the model boundaries and changes its path with the growth of the structure (although not totally correct), it is safe to conclude that the SW location of the source is correct. The next step was to try to reduce the flow down so that it does not cross the structure. Gradually, the size of the source was reduced from approximately seven (7) to three (3) cells. Although the flow was diminished, it was still crossing the structure.

As mentioned in section 3.2.4, the water supply curve depends on a delta time element that is the internal computational time step helping the particles in the flow to settle down (Schlumberger, 2016). Because the computational time step controls how much time takes to the flow to travel across each cell, reducing this parameter makes the flow more stable.

Although the value for this parameter is found by dividing the flow velocity by the cell length (e.g. It takes 36 s for the flow to travel across the cell for a flow velocity of 50 km/h and a 500 m cells length), the computational time is usually smaller than the value calculated with

this relationship. The GPM manual considers (for flow velocity 50 km/h and a 500 m cells length) that an appropriate value is not 36 s but 10 s (Schlumberger, 2017).

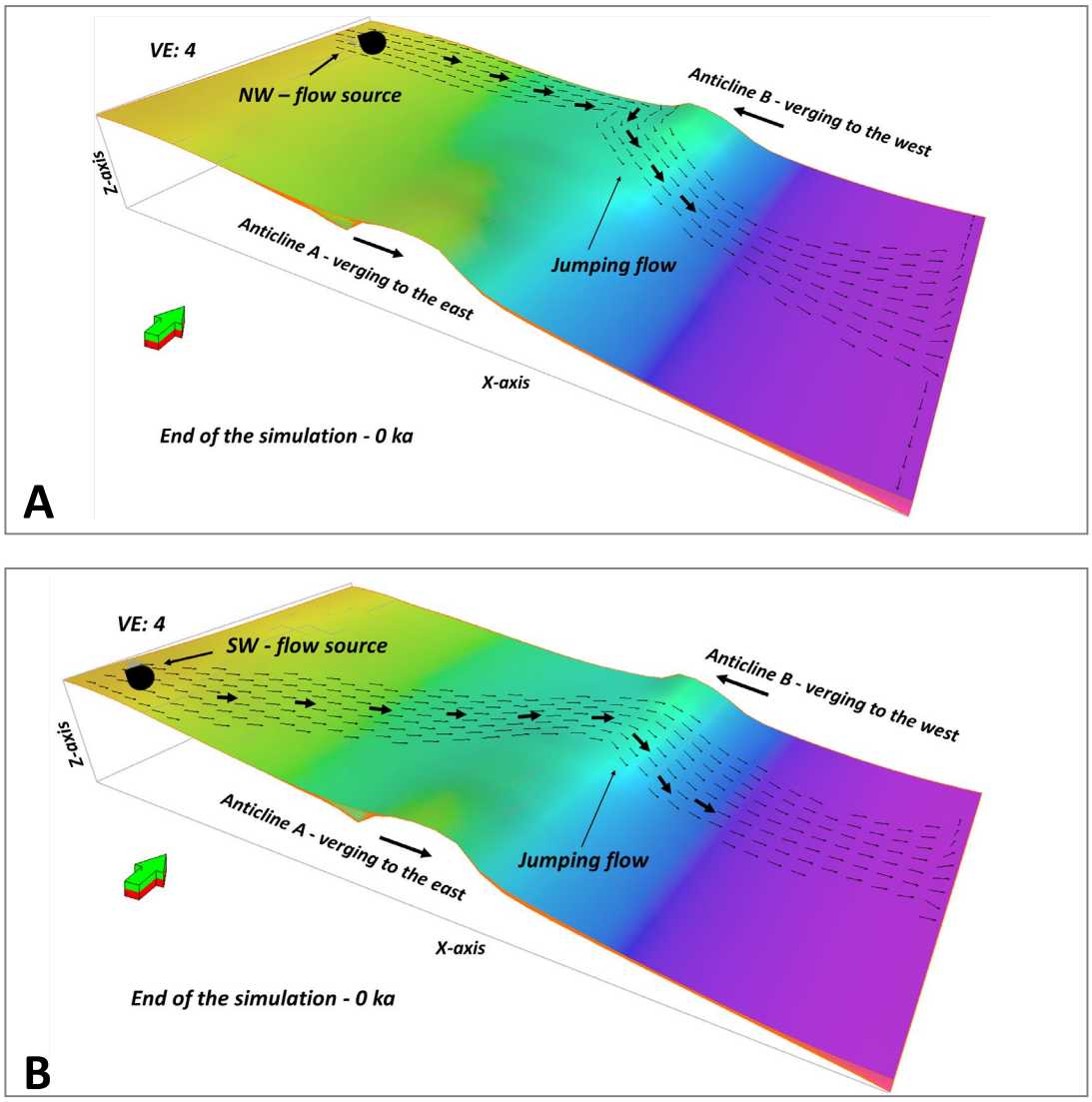

Figure 13. Flow path crossing the structure at the end of the simulation. A. Flow path behavior with a NW flow source location. B. Flow path behavior with a SW flow source location. The colors mean depositional depth varying from shallow (green) to deep (purple). Green arrows point north.

For that reason and due to the uncertainty in the calculation, the best value for this parameter was chosen by trial and error. Always considering (based on several trial and error simulations) that usually, the flow needs more time to traverse the cell and settle down.

Therefore, a small value is commonly required. The disadvantage is that testing the sensitivity of this parameter is time-consuming. Therefore, I choose a range between 0.1 and 0.001 s. After testing several values within the range above, the best value is 0.001 s. For this time, the flow path is correctly diverted towards a topographic low point when reaching the growing structure (Figure 14).

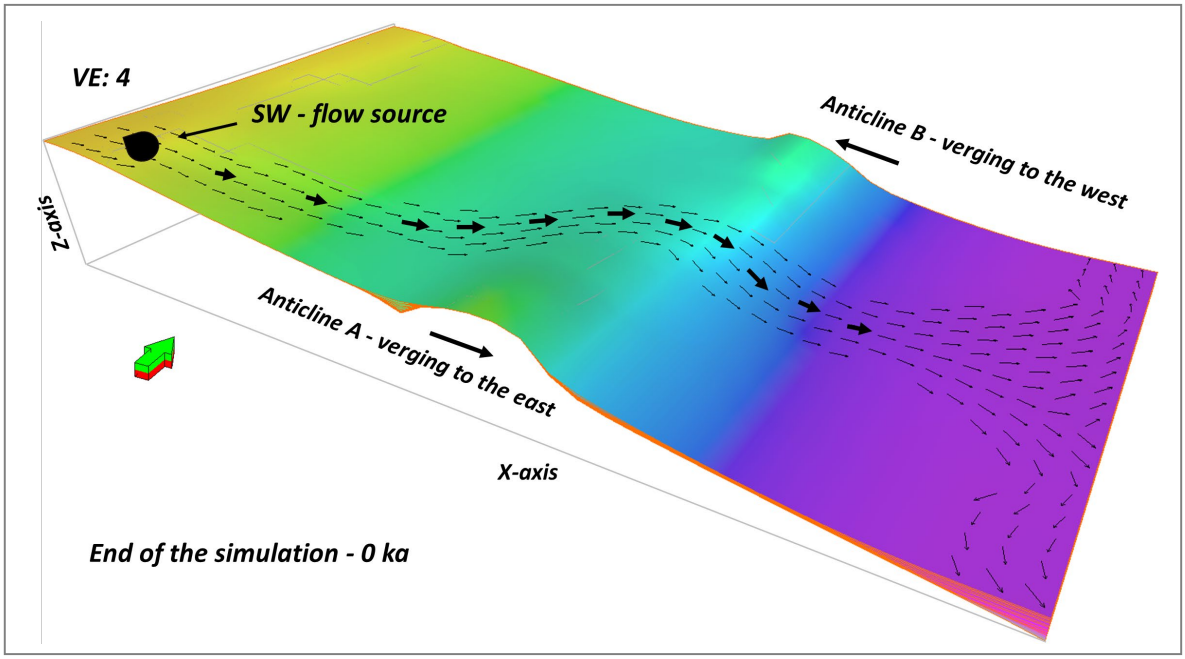

Figure 14. Flow path is modified by the growing structure and is shifted towards a topographic low point. The colors mean depositional depth varying from shallow (green) to deep (purple). The green arrow points north.

Based on these three cases, the parameter ranges that work reasonably were used to create a base model. On this base model, diffusion and unsteady flow were simulated considering different scenarios where the growth of the thrust-related bi-vergent anticlines vary. The growth and the thrust position variation are controlled by the trishear model parameters (e.g., the center of curvature, propagation to slip ratio, among others). Diffusion and unsteady flow were slightly adjusted depending on the model scenario, and the resulting sediment distribution was described and analyzed.

4. Results

Table 2 shows the set of models investigated and the model parameters varied.

4.1 Base model

This case models two listric, opposite-verging thrusts with a center of curvature (CC) defined for the thrust A by X (measured from the west end) = 900 m, and for the thrust B by X = 1600 m, and Z (up) = 150 m. The radius of curvature (CCR) defines how deep the thrust detachment is. This value is set to 300 m. Thus, the thrust detachment (CCZ – CCR) is at -150 m. The initial surface elevation is -20 m (20 m below sea level), and the surface dips 2° toward the east. The grid consists of 41 cells in X and 21 cells in Y, each cell of size 50 x 50 m. The model is run over a time interval of 100 ky, with a display interval of 10 ky. Therefore, the simulation generates 10-layer boundaries.

For the base model, the default trishear parameters are used (Table 2). PS and trishear angle are constant along the thrusts, while the slip rate is maximum at one tip (southern tip in east-vergent thrust, northern tip in west-vergent thrust) and decreases linearly along strike (N) to zero over the N distance of the grid (1 km). This results in two anticlines of opposite vergence, which die along strike (Figure 15). The transfer area between these anticlines as observed in the lowermost horizon of the model (initial surface) at the end of the simulation is about 700 m (Figure 15).

For both the east-vergent and west-vergent anticlines, in the forelimb of the anticlines a relatively gentle slope is generated with thin syn-growth strata in the southern (east-vergent) structure and moderate to thick syn-growth strata in the northern (west-vergent) structure. Syn-growth sedimentary layers are folded over the structures and display significant thinning onto the crest of the anticlines (Figure 16).

Table 2. Sets of models investigated in this thesis. CC: Center of curvature, P/S: Fault Propagation to slip ratio, TA: trishear angle. Cases 1 – 4 and 7 maintain constant TA (60°) and P/S (2.5), while varying CC in X. Cases 5 and 6 maintain constant CC in X (A = 1000 m, B = 1400 m), while varying P/S and TA, respectively. Case 7 center of curvature is as in case 1.

Purpose	Case No.	Text section	Dimensions	Variable Parameter		Main Result
Understand if the anticlines location, the extension of the model boundaries, the propagation to slip ratio (P/S) and the trishear angle (TA) variation favor the deflection and blocking of the flow pathway and enhance the sand-rich sediment deposition.	1	4.1	Initial surface: -20 m Dip: 2° E Cells X: 41 Cells Y: 21 Grid Size: 50 x 50 m	Thrust A - (CC in X) Thrust B - (CC in X)	900 1600	The flows pathway is deflected through time.
	2	4.2	Initial surface: -20 m Dip: 2° E Cells X: 41 Cells Y: 21 Grid Size: 50 x 50 m	Thrust A - (CC in X) Thrust B - (CC in X)	1000 1400	The flows pathway is deflected through time.
	3	4.3	Initial surface: -40 m Dip: 2° E Cells X: 47 Cells Y: 33 Grid Size: 50 x 50 m	Thrust A - (CC in X) Thrust B - (CC in X)	1600 1800	The flows pathway is deflected through time and blocked and deflected at the end of the simulation. The blocking enhances the deposition of sand-rich layers against the northern anticline.
	4	4.4	Initial surface: -40 m Dip: 2° E Cells X: 41 Cells Y: 21 Grid Size: 50 x 50 m	Thrust A - (CC in X) Thrust B - (CC in X)	1300 1200	The flows pathway is deflected through time.
	5	4.5	Initial surface: -40 m Dip: 2° E Cells X: 41 Cells Y: 21 Grid Size: 50 x 50 m	Thrust A - (P/S) Thrust B - (P/S)	4.0 2.5	The flows pathway is deflected through time and blocked and deflected at the end of the simulation. The blocking enhances the deposition of sand-rich layers against the northern anticline.
	6	4.6	Initial surface: -40 m Dip: 2° E Cells X: 41 Cells Y: 21 Grid Size: 50 x 50 m	Thrust A - (TA) Thrust B - (TA)	60° 40°	The flows pathway is deflected through time and blocked and deflected at the end of the simulation. The blocking favor the deposition of sand-rich layers against the northern anticline.
	7	4.7	Initial surface: -20 m Dip: 2° E Cells X: 41 Cells Y: 21 Grid Size: 50 x 50 m	Timestep	2 ky	Sediment distribution pattern due to diffusion and unsteady flow show more sediment mixtures when compared with the Case 1 model (10 ky timesteps).

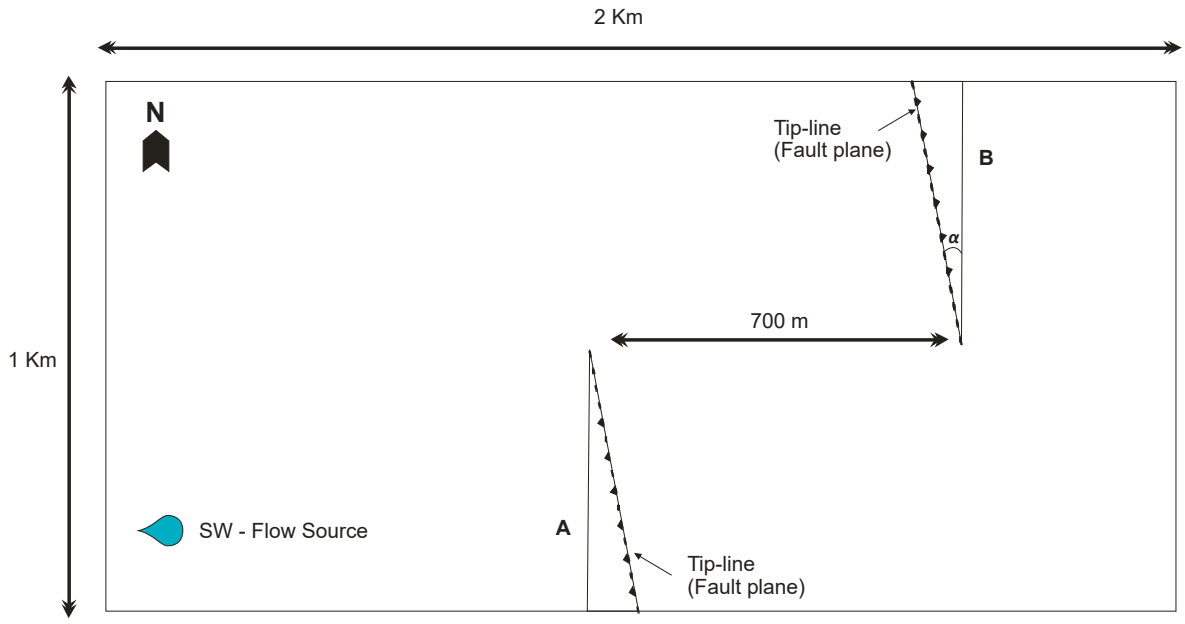

Figure 15. Map view of the base model as observed in the lowermost horizon at the end of the simulation. The opposite-verging thrusts, the transfer zone between them, and the flow source position are indicated.

As described in section 3.2.2, four different lithologies are included in the model: coarse sand (red), fine sand (green), silt (blue) and clay (black). Over time, sediments are diffused downhill but with different intensity. At the start of the simulation (100 - 80 ka), the eroded sediments come mainly from the top of the slope (western edge or shallower area, Figure 16A). Since the source is located at the SW corner, the transport and erosion of the sediments is not the same along the north. Towards the NW, sediment transport just depends on diffusion (sediment size and density) and a slow downhill advance is observed. As expected, the coarse-size sediments are located closer to the slope, while the fine-size sediments, travel farther east (Figure 16A). Towards the SW, sediment transport depends on both diffusion and unsteady flow. In this sector, sediment distribution depends more on the flow path. Since the flow is strong enough, it can carry coarse sediments to areas further east and a marked coarse sand path is distinguished from west to east (Figure 16A).

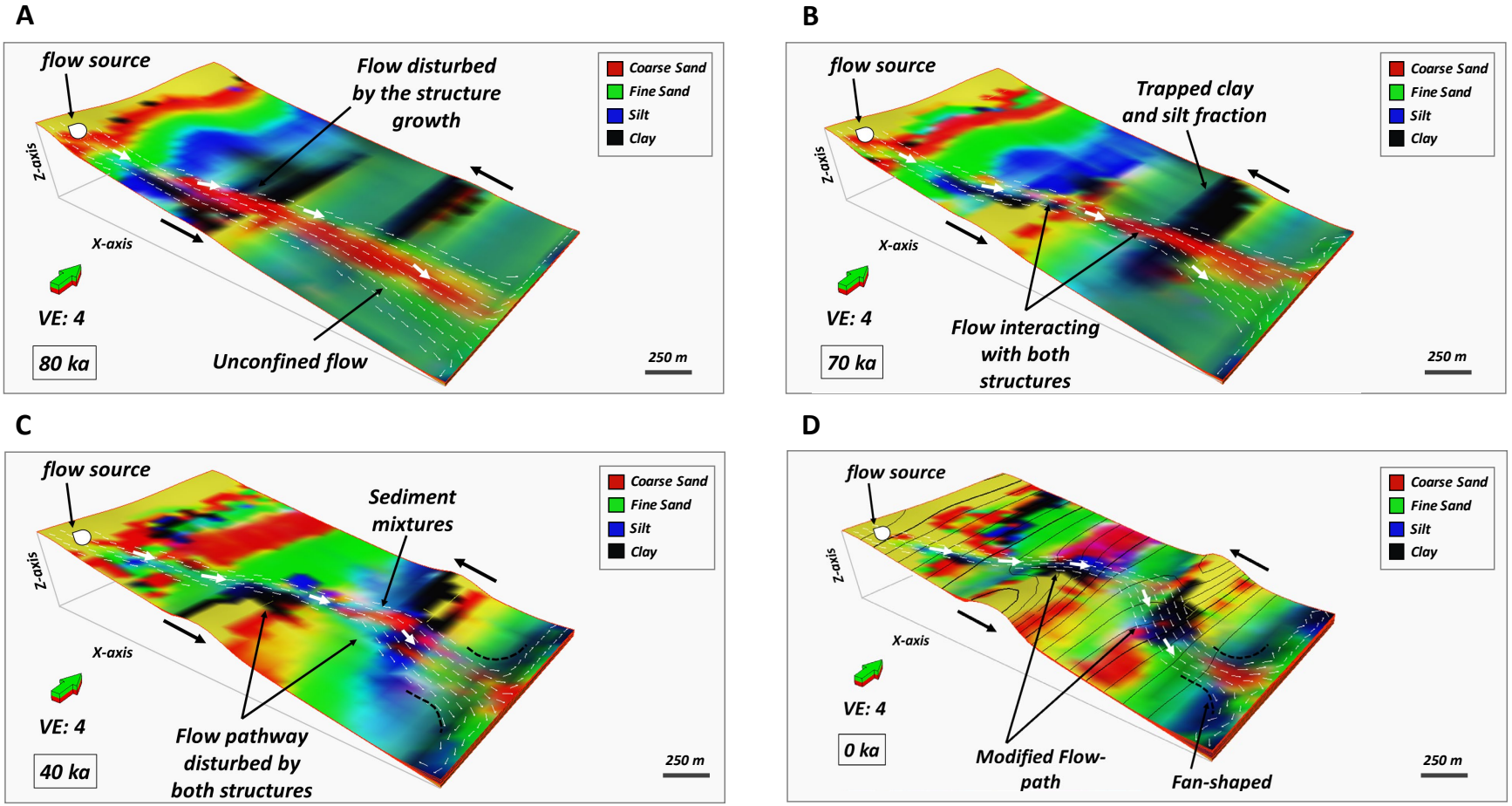

Figure 16. Base Model. A, B, C, and D show the flow path and the sediment distribution at times 80 ka, 70 ka, 40 ka, and 0 ka, respectively. Green arrows point north. White arrows indicate the flow direction. Black arrows show the vergence of the anticlines. The colors indicate the modeled lithologies: coarse sand (red), fine sand (green), silt (blue) and clay (black). The figures have a vertical exaggeration of 4.

At 80 ka (Figure 16A), the flow starts to be deflected towards the north by the southern (east-vergent) growing anticline. The unconfined flow spreads radially before it overpasses the southern (east-vergent) structure. At 70 ka (Figure 16B), the flow continues its path towards the north and starts to interact with both southern (east-vergent) and northern (west-vergent) anticlines. The flow is laterally confined by the growing southern structure and spreads radially before reaching the northern structure. Towards the north (diffusion dependent side), coarse-size sediments are observed near the slope and fine-size sediments farther east. Here, the clay fraction (black color) travels long enough to reach the northern (west-vergent) structure, where it is trapped. Towards the south, sediment distribution is still controlled by the unsteady flow. However, with growth of the southern (east-vergent) anticline, erosion due to diffusion is now exhibited. Coarse sediments are deposited in the forelimb and some clay sediments on the backlimb of the southern (east-vergent) anticline.

At 40 ka (Figure 16C), the flow is greatly influenced by the growth of the anticlines,which modify its path. The sediments carried by the flow are mixed with the sediments eroded from the anticlines. After overpassing the northern anticline, the flow becomes unconfined and spreads laterally. It has a markedly SE direction due to the influence of the northern structure. Continuous migration of the flow towards the SE, spreads fine and coarse sand material and generates a fan with an asymmetric geometry in cross section.

At the end of the simulation (0 ka, Figure 16D), the final sediment distribution can be observed. One of the most notable features is the distribution of the finer sediments (black and blue) along the crest of both anticlines. This thin layer of fine sediments remains trapped in the crest of the anticlines but it is transported along strike towards lower relief (less slip) areas. The other notable feature is how the flow path is deflected by the structures and the sediments that constitute the fan migrate towards the SE. Notice that the flow has reduced its

size and capacity to transport coarse-size sediments. In the upper part of the fan (Figure 16 D, towards the ESE boundary of the modeled area), coarse-size sands are deposited, while in the upper-middle part, coarse and fine sands are deposited. Since the modeled area is not large enough, it is not possible to observe the whole fan development, but the extension of it can be inferred. In general, in this simulation, unsteady flow leaves patches of coarse-size sediments in their path when it migrates, while sediments that are diffused advance downhill in a linear pattern until they find a surface disturbance that impedes their travel.

4.2 Closer anticlines, narrower transfer area

This case models two listric, opposite verging thrusts with a center of curvature (CC) defined for the thrust A by X (measured from the west end) = 1000 m, and for the thrust B by X = 1400 m. The CC in Z (up) is 150 m. This model has the same dimensions, number of cells, cell size and initial surface elevation than the base model (section 4.1). The display interval is 10 ky over a total period of 100 ky (10 layers are generated), the anticlines die out along strike over a distance of 1 km, and the source area is located to the SW.

A narrower transfer zone is the only parameter that varies. This transfer area is dominated by two thrust-related anticlines of opposite vergence, spaced 400 m in the lowermost horizon of the model (initial surface) at the end of the simulation (Figure 17). As in the base case, moderate to thin layers that onlap the structures constitute the syn-growth strata. Towards the east (basin location) the syn-growth layers increase considerably in thickness (Figure 17).

Since the source for the unsteady flow is located at the SW corner, the southern area is influenced at the beginning of the simulation by unsteady flow and diffusion, while the northern area is influenced entirely by diffusion. When the simulation starts, the sediments in the north are eroded and deposited depending on their grain size and density; coarse-size

sediments are deposited near the slope while fine-size sediments reach distances farther east. In the southern area, the sediments are transported longer distances following the flow path which leaves a clear coarse sand trend.

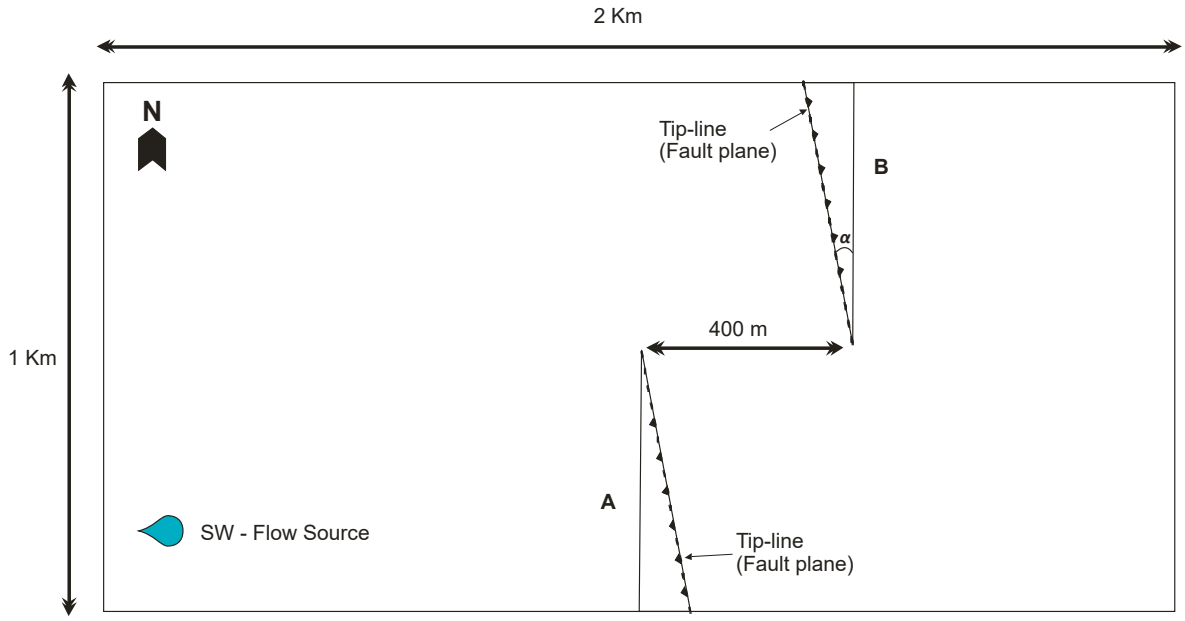

Figure 17. Map view of case 2 (narrower transfer zone) as observed in the lowermost horizon at the end of the simulation. The opposite verging thrusts, the transfer area between them, and the flow source position are indicated.

At 60 ka (Figure 18A), the flow path is modified by the southern (east-vergent) structure and the coarse sediments carried by the flow begin to migrate towards the north (flow direction). Diffusion takes place and the sediments eroded from the southern structure are added to the flow. Towards the east, the flow carries sediments that are deposited in a weak fan. Notice that the flow behaves as unconfined and spreads laterally almost reaching the eastern boundary. At 40 ka (Figure 18B), the flow starts to interact with the northern (west-vergent) structure, and the sediments start to be eroded from the backlimb of this anticline. In the southern anticline, sediments eroded from the forelimb are mixed with sediments transported

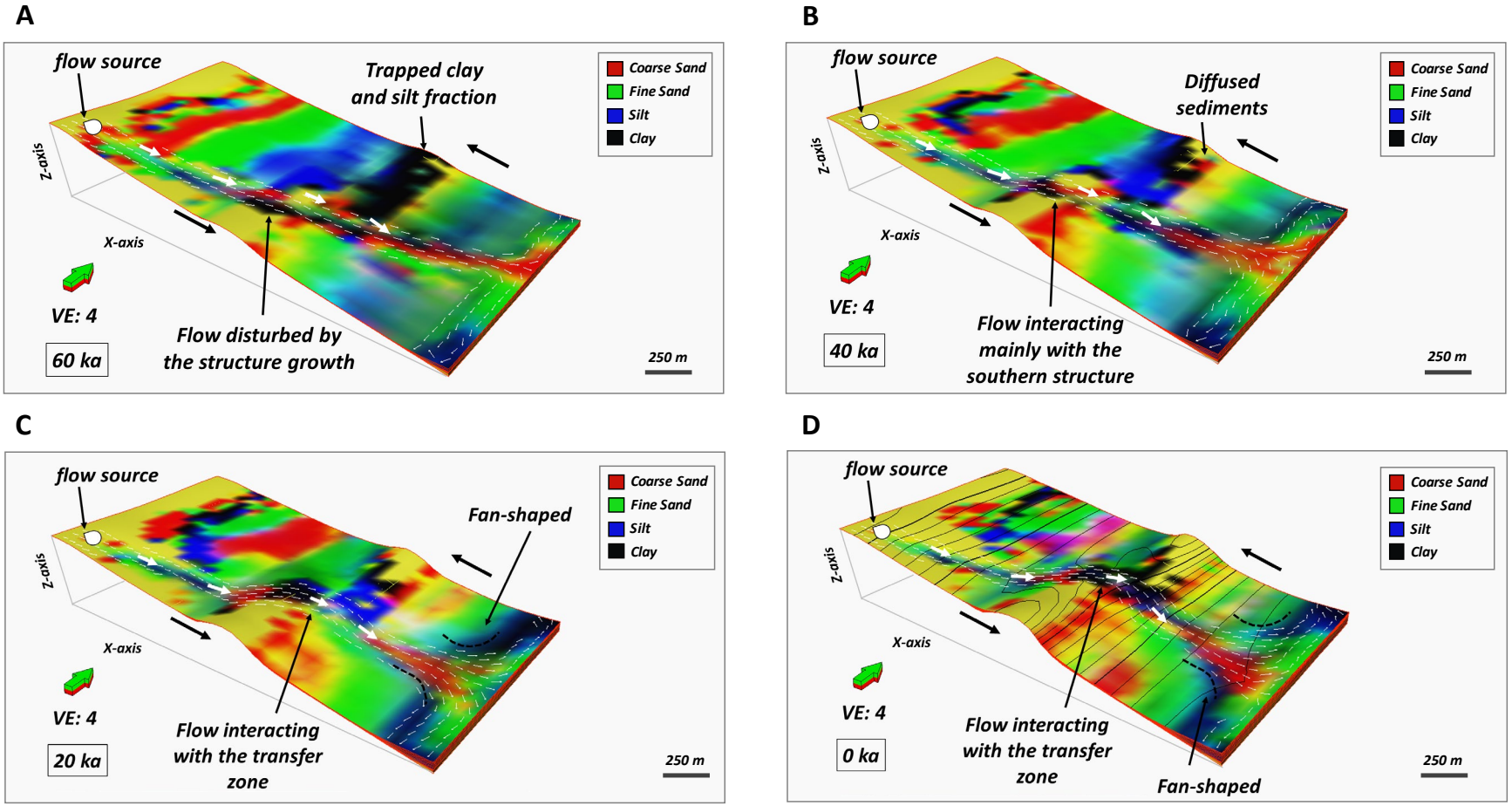

Figure 18. Case 2 – Narrower transfer zone. A, B, C, and D show how the flow path and the sediment distribution vary at times 60 ka, 40 ka, 20 ka, and 0 ka, respectively. Green arrows point north. White arrows indicate the flow direction. Black arrows indicate the anticlines' vergence. The colors indicate the modeled lithologies: coarse sand (red), fine sand (green), silt (blue) and clay (black). The figures have a vertical exaggeration of 4.

by the flow. Note that the flow has increased its size and a more defined fan can be distinguished towards the NNE (preferential deposition direction of coarse sand). At 20 ka (Figure 18C), the flow is entirely modified by the anticlines and it concentrates on the lower (dying) parts of them. Diffusion modifies the anticlines and coarse-size sediments are deposited near their limbs, while fine-size sediments advance towards the eastern boundary of the model. The fan produced by the main flow is clearer, and at least two well-defined channels can be identified. The coarse sediments in these channels are a mix between coarse and fine sand (red and green colors, respectively). At the end of the simulation (0 ka, Figure 18D), the flow spreads laterally after overpassing the northern anticline. The flow adds more sediment coming from the transfer zone between the anticlines, and a marked but asymmetric upper fan of coarse sediments towards the east is recognized.

A cross-section through the northern (west-vergent) structure shows in detail these features (Figure 19A). Fine sediments (clay and silt) eroded from the shallowest part of the model (western boundary) are transported longer distances before being trapped on the anticline forelimb. Coarser sediments in the forelimb of the anticline are deposited later when the structure is high enough to be eroded. A stack profile near the structure will show finer sediments towards the base and coarser sediments towards the top, but far from the structure (towards the west) the fine-size sediments decrease and are mostly confined to the base. Coarse-size sediments will be found towards the top, as an intercalation of coarse and fine sand. On the other hand, the backlimb of the fold shows a normal sediment distribution, which consists of coarse-size sediments on the source vicinity and fine-size sediments towards the basin (eastern model boundary).

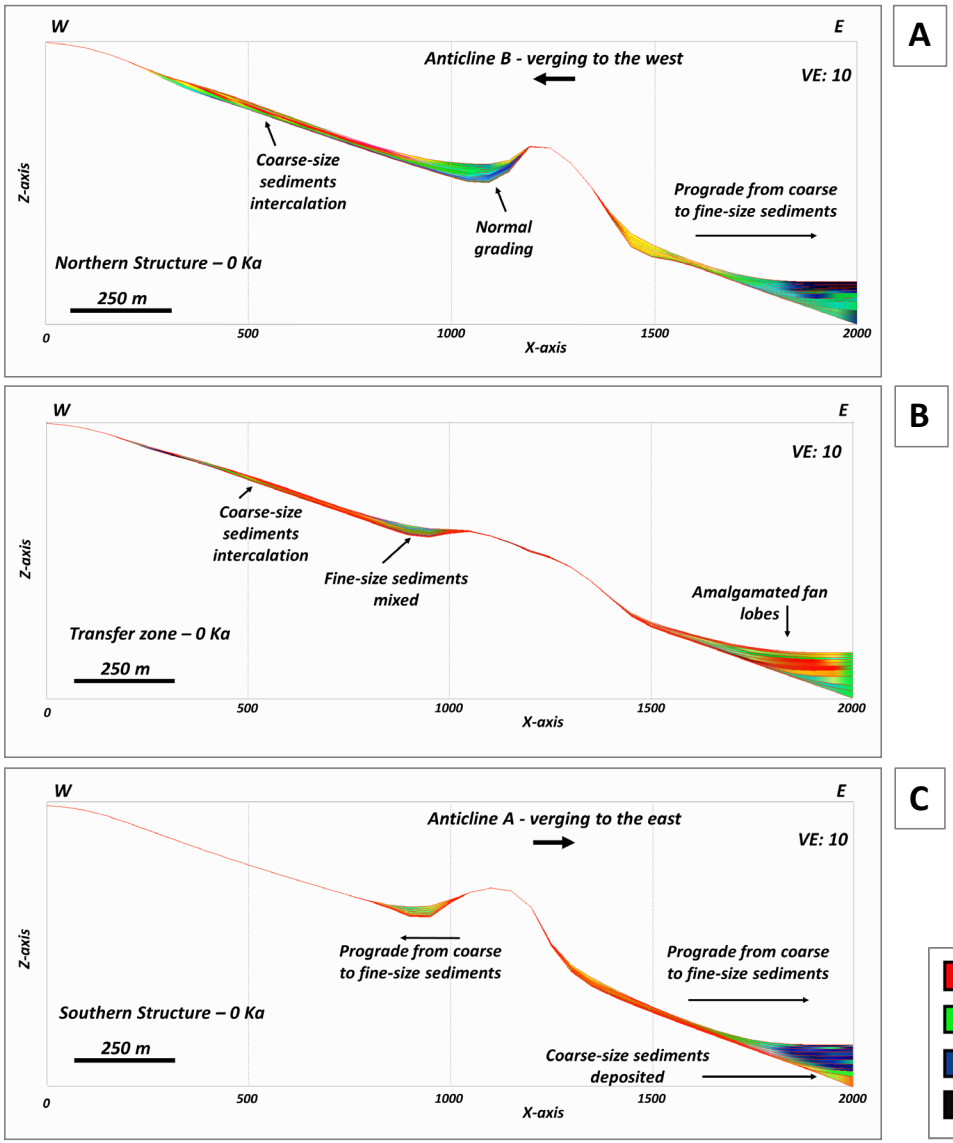

Figure 19. Cross-sections through the modeled area showing the sediment distribution pattern from west to east at the end of the simulation. A. Cross-section across the northern structure. B. Cross-section across the transfer zone. C. Cross-section across the southern structure. The colors indicate the modeled lithologies: coarse sand (red), fine sand (green), silt (blue) and clay (black). The sections have a vertical exaggeration of 10.

Across the transfer zone, the same pattern observed in the north develops (Figure 19B). Towards the west near the transfer zone, during the first simulation cycles, fine-size sediments (clay and silt) are deposited, which are trapped by the emerging structure. At the top, these sediments are mixed mostly with fine sand. Farther west from the transfer zone, fine size sediments are observed at the base, but coarse-size sediments with thin intercalations of silt and fine sand predominate at the top. Towards the east, the sediments are mainly transported by the unsteady flow, so coarse-size sediments predominate. Here, amalgamated sandy fan lobes are controlled by the flow.

The cross-section across the southern (east-vergent) anticline shows a different sediment distribution than the northern anticline (Figure 19C). Here in both the backlimb and forelimb of the anticline, sediments prograde from coarse to fine. This follows the typical diffusion distribution, with coarse-size sediments near the source and fine-size sediments far from it. However, towards the basin (eastern boundary) and during the first simulation cycle, the sediments are preferably coarser.

For this case, a higher-resolution simulation was performed (Figures 20 and 21). The trishear model parameters and the initial surface elevation is the same, but the grid consists of 81 cells in X by 41 cells in Y, each cell of size 25 x 25 m. The display interval and total time are the same (10 and 100 ky) and 10-layer boundaries are generated.

The main difference between the high and low-resolution models, is that in the high-resolution model, the sediments boundary and the flow path are defined better (Figure 20). But in general, the sediment distribution of low- and high-resolution models is the same when the cross-sections are analyzed (Figure 21). In general, the sediment distribution does not radically change when reducing the cell size by half. However, in the cross section across the transfer zone (Figure 21B), the amalgamated sandy fan lobes controlled by the flow and

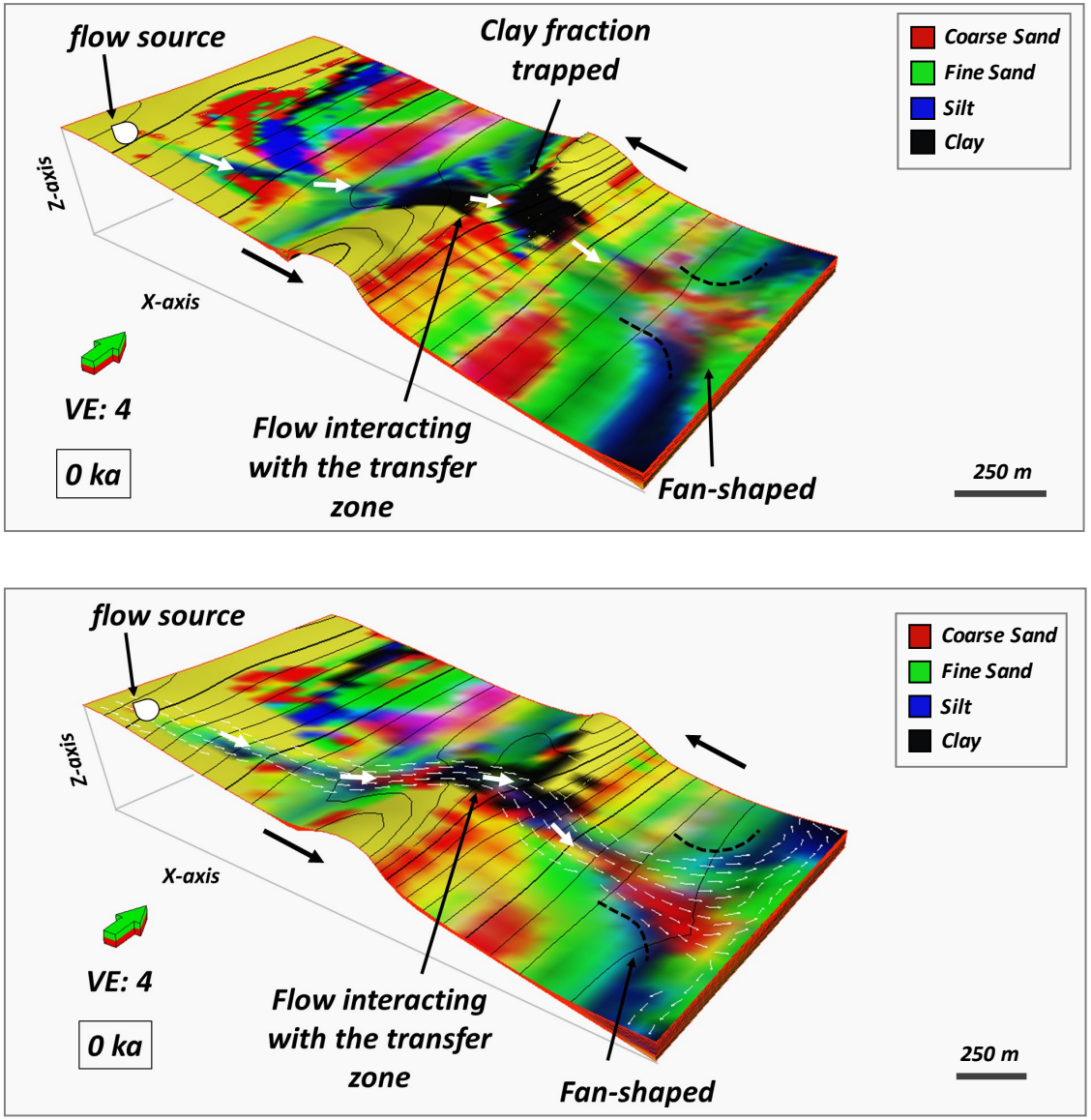

Figure 20. Case 2 – Narrower transfer zone. Comparison between the sediment distribution of the high-resolution model with cells 25 x 25 m (A), and the low-resolution model with cells 50 x 50 m (B). Green arrows point north. White arrows indicate the flow direction. The colors indicate the modeled lithologies, Coarse sand (red), fine sand (green), silt (blue) and clay (black). The figures have a vertical exaggeration of 4.

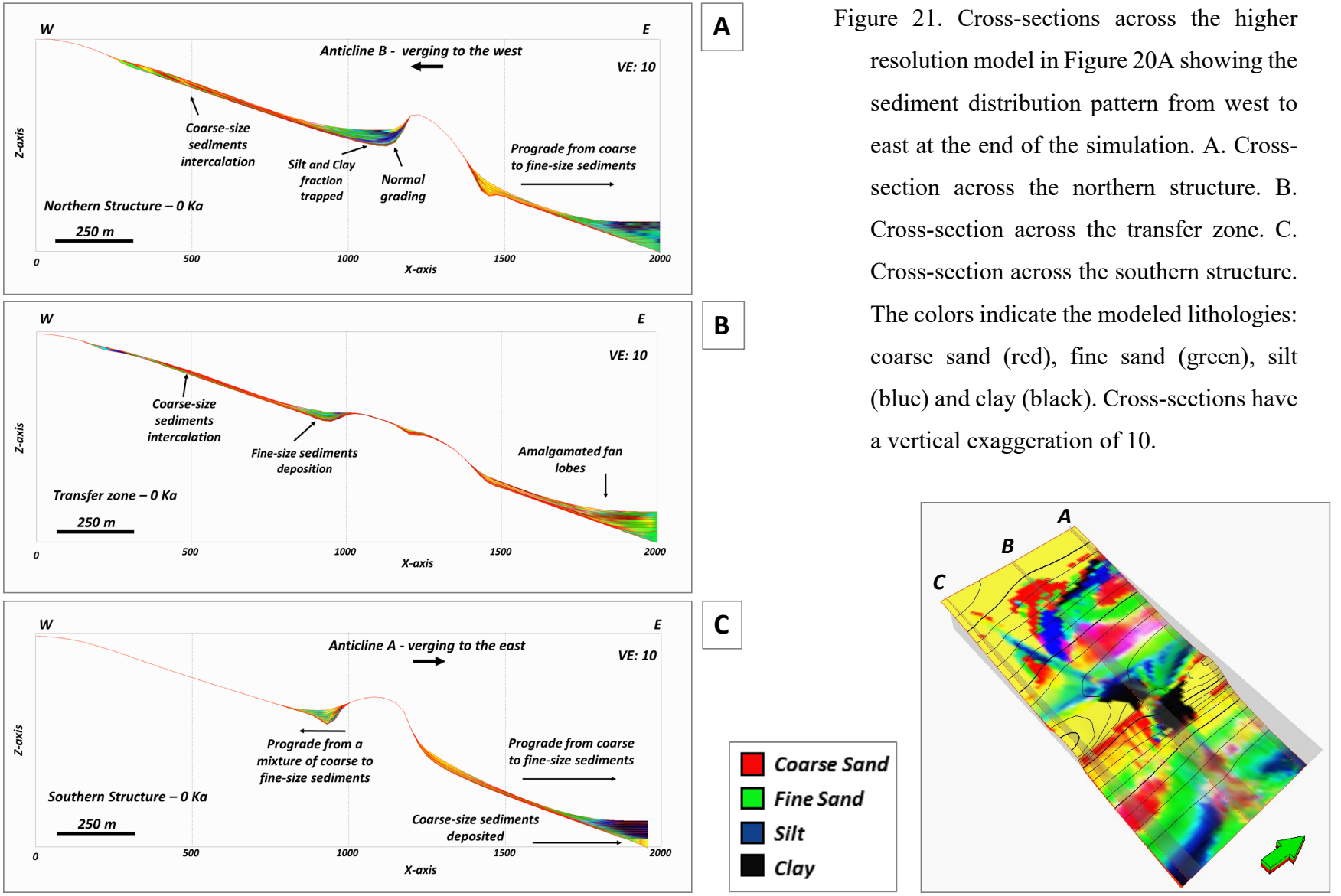

Figure 21. Cross-sections across the higher resolution model in Figure 20A showing the sediment distribution pattern from west to east at the end of the simulation. A. Cross-section across the northern structure. B. Cross-section across the transfer zone. C. Cross-section across the southern structure. The colors indicate the modeled lithologies: coarse sand (red), fine sand (green), silt (blue) and clay (black). Cross-sections have a vertical exaggeration of 10.

deposited towards the eastern boundary, do not show a uniform sediment distribution. Since the flow increases it size, it adds more sediments coming mainly from the northern structure, and therefore an increase in sediment mixtures in the higher resolution model is noticed.

4.3 Colinear anticlines with extended model boundaries

This case models two listric, opposite verging thrusts with a center of curvature (CC) for the thrust A in X (measured from the west end) = 1600 m, and for the thrust B in X = 1800 m, and Z (up) = 150 m for both thrusts. These centers of curvature make the structures almost colinear along N-S (Figure 22). The initial surface is located 40 m below sea-level and dips 2° toward the east. The grid consists of 47 cells in X and 33 cells in Y, each cell of size 50 x 50 m.

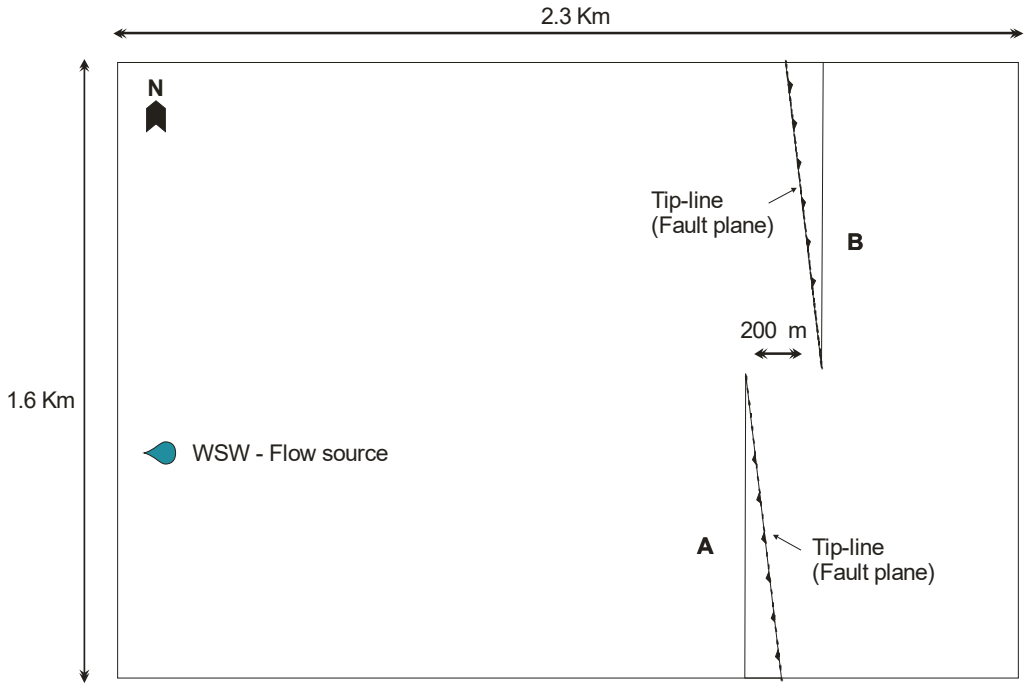

Figure 22. Map view of case 3 (colinear anticlines with extended model boundaries) as observed in the lowermost horizon at the end of the simulation. Thrusts and the flow source position are indicated.

To avoid the flow spreading outside the modeled region at the early stages of the simulation, the model has extended boundaries, 2.3 km long along E-W, and 1.6 km wide along N-S (Figure 22). The display interval is the same than the base model (section 4.1). For this case, the flow source is in the WSW boundary (Figure 22).

For both the east-vergent and west-vergent anticlines, the model generates at the backlimb of the fold, a thin but sharp syn-growth sedimentary wedge. In contrast to the backlimb, in the forelimb of the anticlines a relatively gentle slope is generated with thin syn-growth strata in the southern (east-vergent) structure and moderate to thick syn-growth strata in the northern (west-vergent) structure. Syn-growth sedimentary layers are folded over the structures and experience significant thinning onto the crest of the anticlines (Figures 23D, 24A and 24C).

The structures begin to confine and divert the flow between 80 and 70 ka (Figure 23A). Again, the fine size sediments (silt and clay) are trapped by the growing structures. At this time, coarse sand (red color) erosion in the forelimb of the southern (east-vergent) structure and the backlimb of the northern (west-vergent) structure starts. At 40 ka (Figure 23B), the flow starts to modify the zone where the thrust faults link, which has a concave upward shape. The flow behaves as unconfined when it overpasses the northern and southern structures. Diffusion continues eroding and depositing coarse-size sediments (red to green colors) near the source and fine-size sediments (blue to black colors) far from it. Unsteady flow continues to carry mainly coarse-size sediment towards the basin (eastern boundary), where an upper-fan with three well-defined channels of coarse sand (red color) is distinguished. Notice, that the flow size increases when the anticlines are overpassed,

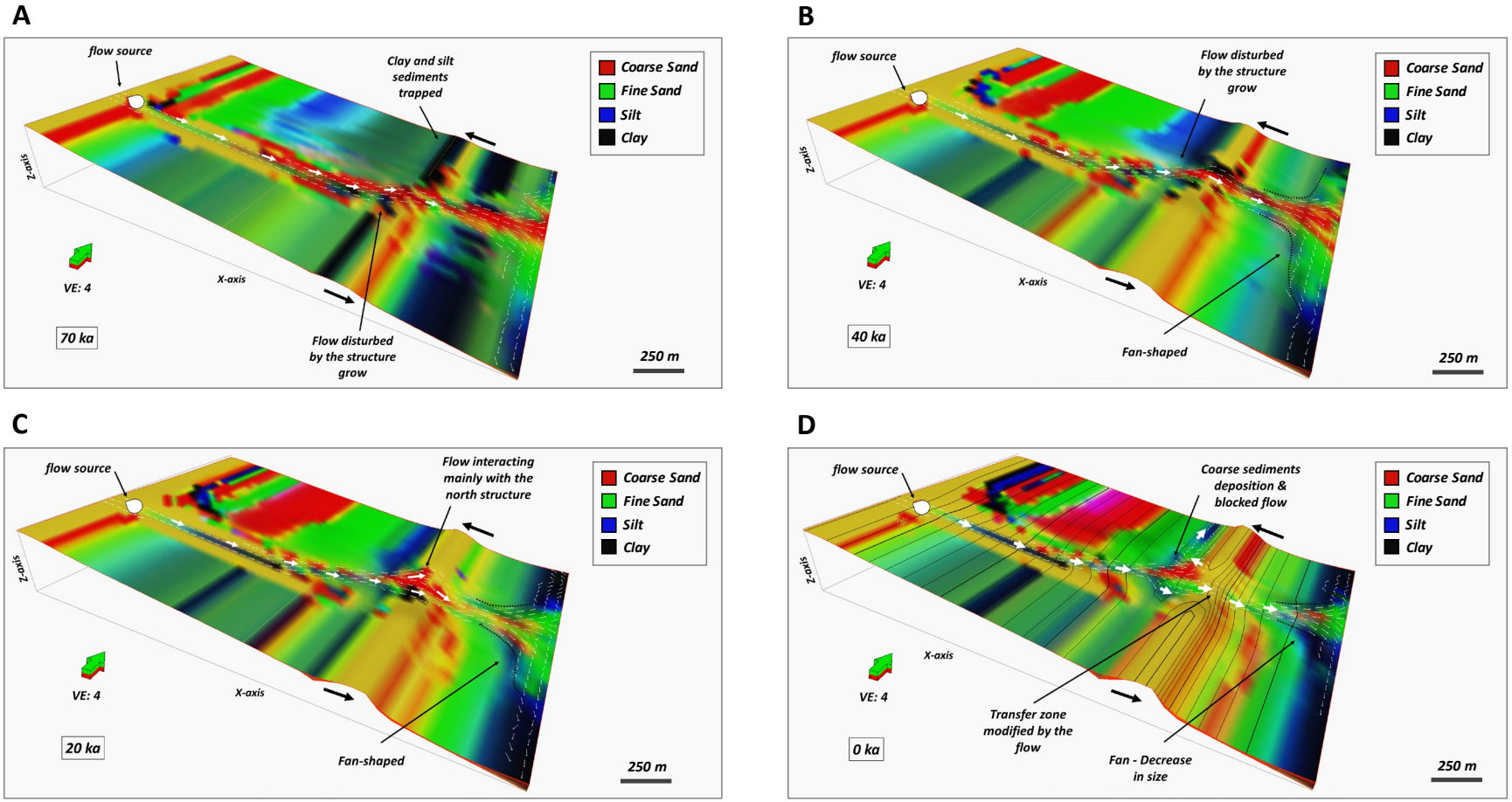

Figure 23. Case 3 – Colinear anticlines with extended model boundaries. A, B, C, and D show the flow path and the sediment distribution at 70 ka, 40 ka, 20 ka, and 0 ka, respectively. Green arrows point north. White arrows indicate the flow direction. Black arrows indicate the anticlines' vergence. The colors indicate the modeled lithologies: coarse sand (red), fine sand (green), silt (blue) and clay (black). The figures have a vertical exaggeration of 4.

and behaves as unconfined, similar to the previous stage. At 20 ka (Figure 23C), the flow interacts mostly with the northern (west-vergent) structure. The southern structure is therefore higher than the northern structure. At the end of the simulation 0 ka (Figure 23D), both structures are high enough to block part of the flow which is now totally deflected towards the northern boundary of the model. Sediment distribution for the northern anticline changes and the coarse-size sediments (red and green colors) are deposited against its forelimb. Fine-size sediments (blue to black colors) are deposited as well against the forelimb of the northern structure, but further towards the north. Towards the east, where the flow is less influenced by the structure, a well-defined upper fan is recognized. But at this time, the flow size and the amount of sediments transported to this area have diminished and the sediments are predominantly fine sand (green color).

In the cross-section through the northern structure (Figure 24A), the steep forelimb in the west has predominantly coarse-size sediments towards the top. The adjacent syncline to the west is filled mainly with fine-size sediments that increase in thickness towards the top. The base of the synclinal is a mix between fine sand, silt, and clay but the fraction of fine sand decreases towards the top. Further west, towards the west boundary, the fraction of coarse sediments increases towards the top. At the western boundary, the sediments are predominantly intercalations of fine sand and coarse sand of variable thicknesses. On the other hand, the backlimb to the east is mainly constituted by sandy sediments. Far from the structure towards the east, sediment size decreases towards the top. The sediment varies from fine sand at the base to silt and clay at the top.

In the cross-section north of the transfer zone (Figure 24B), the western side of the structure is mainly composed at the base by a mixture of silt and fine sand sediments, and at the top by amalgamated coarse-size sediments (coarse and fine sand), which increase in thickness

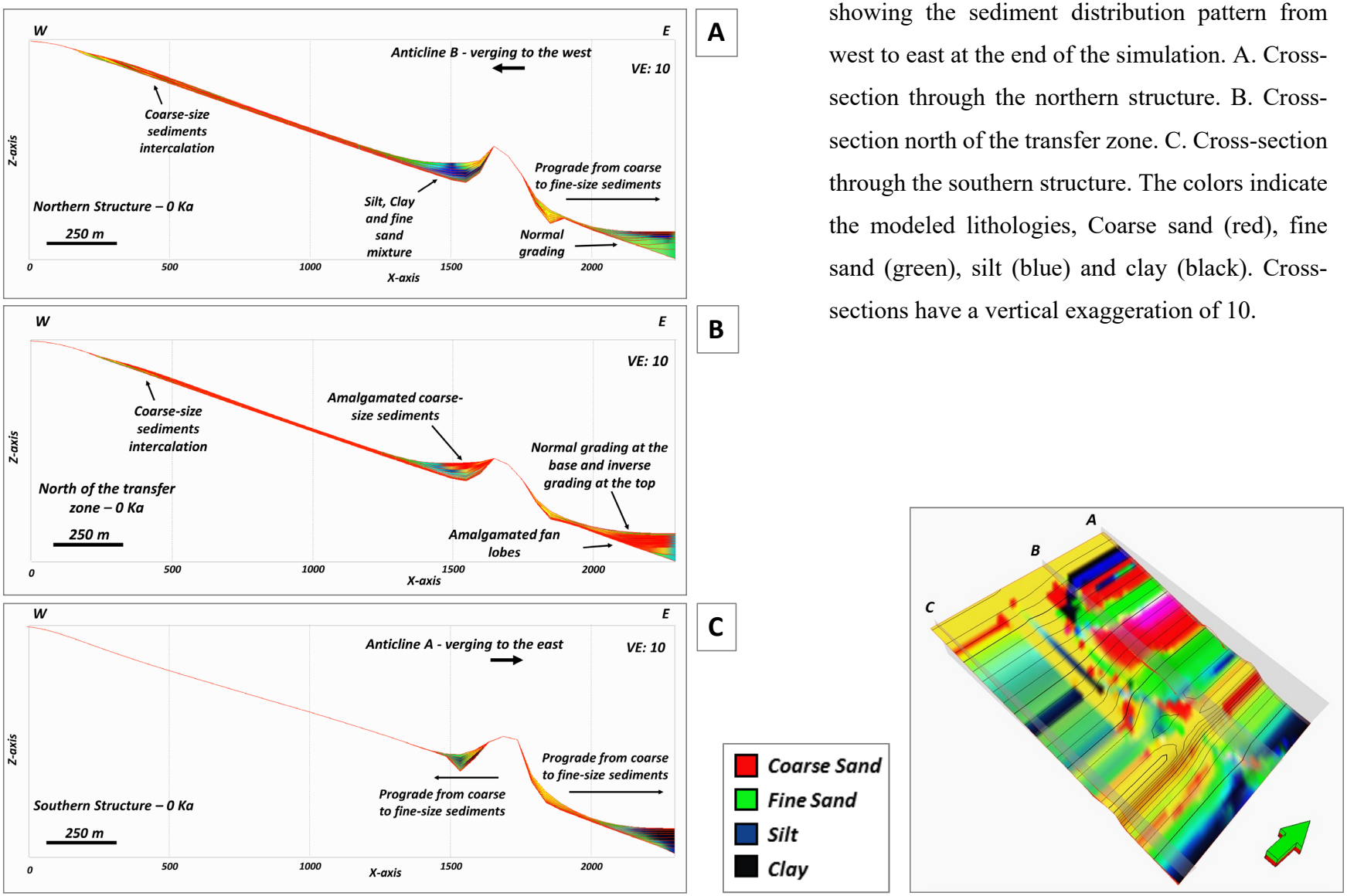

Figure 24. Cross-sections through the modeled area showing the sediment distribution pattern from west to east at the end of the simulation. A. Cross-section through the northern structure. B. Cross-section north of the transfer zone. C. Cross-section through the southern structure. The colors indicate the modeled lithologies, Coarse sand (red), fine sand (green), silt (blue) and clay (black). Cross-sections have a vertical exaggeration of 10.

towards the top. The eastern side of the structure is mainly composed of amalgamated coarse-size sediments (coarse and fine sand) without any clear distribution pattern. At the eastern boundary, it is possible to recognize two different deposition trends from base to top. At the base, the sediments vary from a mixture of fine sand and silt to coarse sand (from blue to red colors). And at the top (last simulation stage), the sediments vary from a mixture of coarse and fine sand to fine sand and silt (from red to blue colors).

The cross-section through the southern anticline (Figure 24C) shows similar sediment distribution pattern than the northern anticline. Here, the main difference is that sediment deposition west of the anticline is almost not present. Towards the east in the forelimb, sediment erosion and deposition are higher, but the sediment distribution pattern is still the same: coarse-size sediments near the forelimb and fine-size sediments far from it.

4.4 Anticlines with switched location

This case models two listric thrusts with a center of curvature (CC) for the thrust A in X (measured from the western end) = 1300 m, and for the thrust B in X = 1200 m. This gives a transfer area of about 100 m, but with the location of A and B switched (Figure 25). The main difference with the previous cases is that the northern structure is located towards the west while the southern structure is located towards the east. This model has the same display interval (10 ky), dimensions, number of cells and cell size than the base model (section 4.1). The initial surface is located 40 m below sea-level and dips 2° towards the east. The source of the flow is located at the WSW boundary (Figure 25).

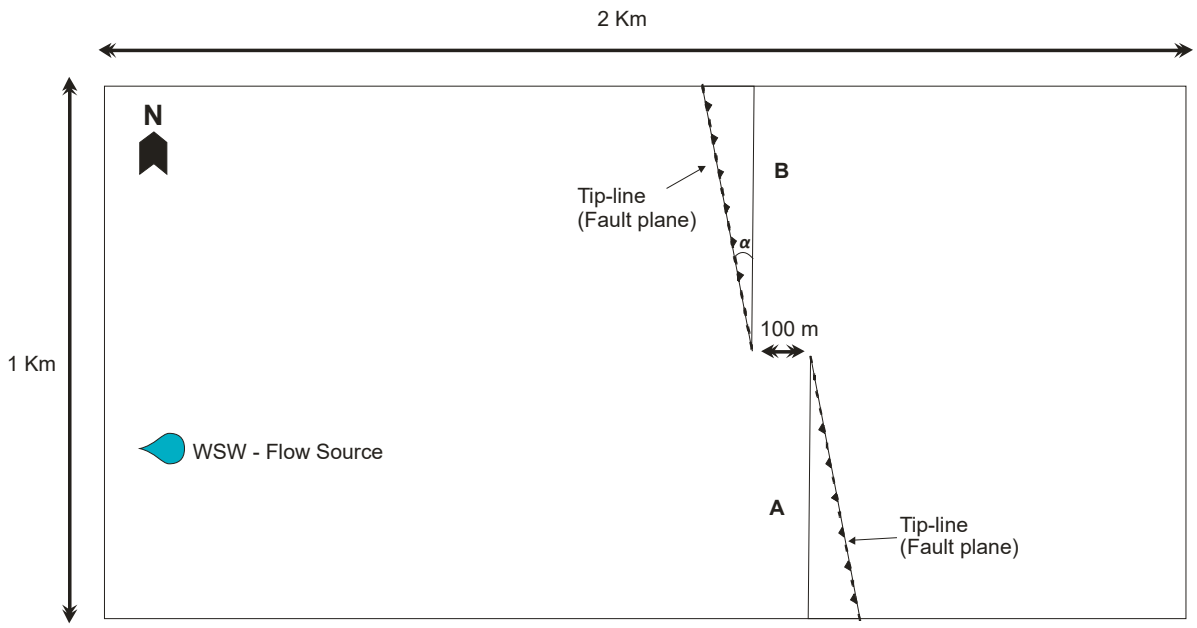

Figure 25. Map view of case 4 (anticlines with switched location and extended model boundaries) as observed in the lowermost horizon at the end of the simulation. Thrusts, the transfer zone between them, and the flow source position are indicated.

At the beginning of the simulation, as in the previous cases, the flow is unconfined and starts to spread radially before reaching the northern structure. However, at 80 ka (Figure 26A), the flow is slightly influenced by the southern (east-vergent) structure. Diffusion acts at the western boundary and, coarse-size sediments (red and green colors) are deposited near the source and fine-size sediments (blue and black colors) far from it. The flow carries mainly coarse-size sediments but different to the other cases, the amount of fine sediments carried by the flow is larger. Like in the previous cases, the fine-size sediments (blue and black colors) are trapped by the emerging structure. At 60 ka (Figure 26B), the flow interacts with both, northern and southern, structures. The southern structure deflects the flow which makes the sediments to be mostly deposited towards the NE. There, a not so well-defined upper fan seems to migrate towards the north. The southern anticline is affected by diffusion and the eroded sediments (coarse sand) are added to the flow. At 30 ka (Figure 26C), the flow is

totally confined by both anticlines and after overpassing the anticlines it behaves as unconfined. The unconfined flow transports mixed coarse-size sediments towards the eastern boundary of the model, and the channel path continues migrating towards the north, which is the preferential direction of the flow. The fan shows at least two well-defined distributary channels that carry mixtures of coarse-size sediments (mainly coarse sand). At the end of the simulation (0 ka, Figure 26D), the southern structure and the transfer zone between the structures has been greatly modified and smoothed by the flow path. At this time, the coarse-size sediments carried by the flow have diminished considerably. The fan is less-defined that in the previous stage and is mainly composed of mixed coarse-size sediments (mostly fine sand).

In the cross-section through the northern structure (Figure 27A), the forelimb towards the west shows the same sediment distribution that in the previous case. The adjacent syncline is filled mostly by mixed fine sand and silt sediments that increase in thickness towards the top. Towards the west, coarse-size sediments mainly consisting of intercalations between coarse sand and fine sand (red and green colors) are deposited. Towards the east, the sediments prograde, changing from a mix of coarse-size sediments to fine-size sediments. The backlimb of the anticline is composed mainly of mixed coarse-size sediments (from red to green colors).

In the cross-section north of the transfer zone (Figure 27B), the sediment distribution is mainly the same from west to east. Towards the west, the sediments are intercalations of coarse and fine sand (from red to green colors). Towards the east, the sediments prograde, changing from coarse-size sediments to a mix of fine sand and little fractions of silt. In general, the whole section consists of coarse-size sediments intercalations.

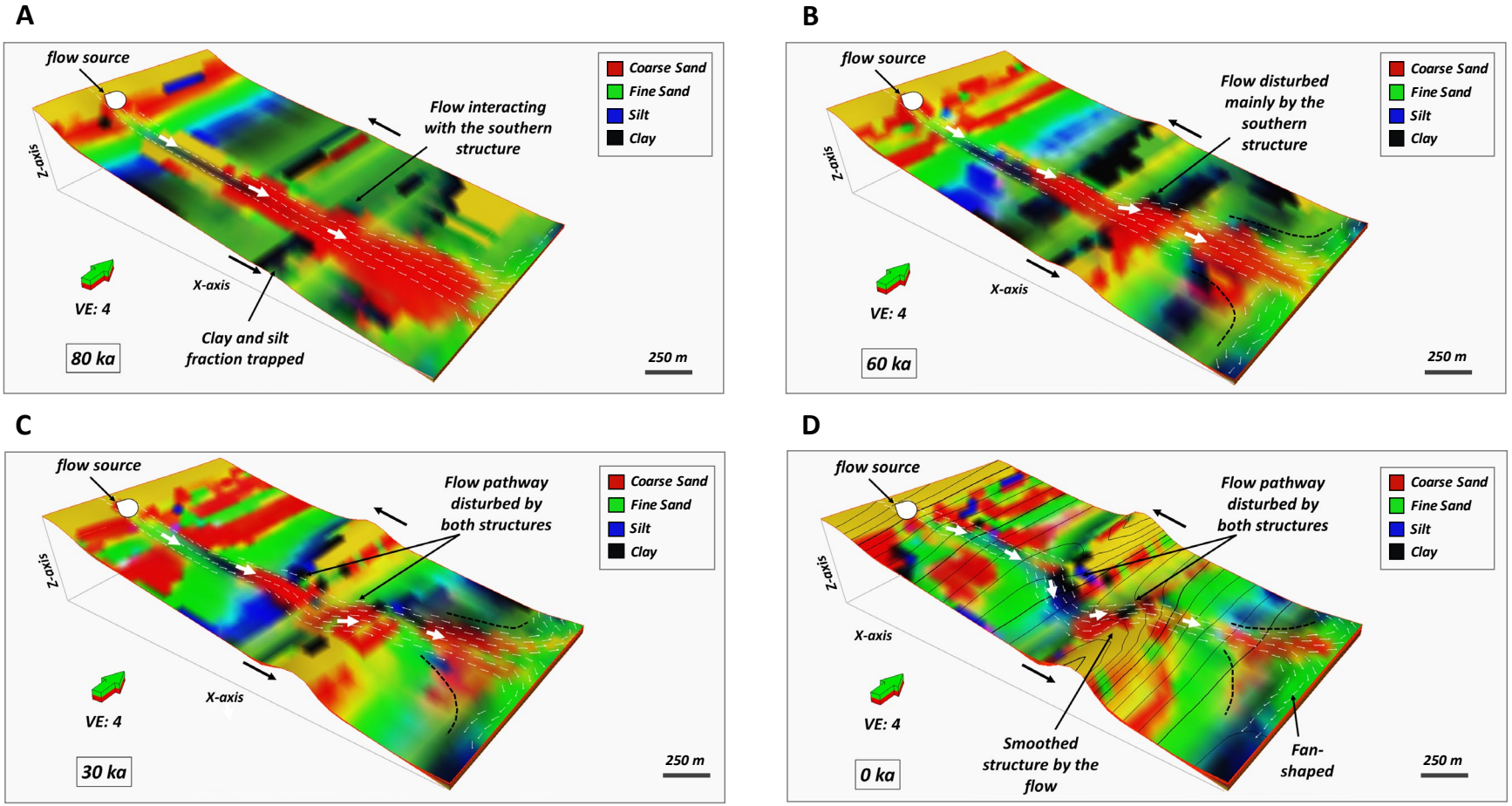

Figure 26. Case 4 – Anticlines with switched location. A, B, C, and D show the flow path and sediment distribution at times 80 ka, 60 ka, 30 ka, and 0 ka, respectively. Green arrows point north. White arrows indicate the flow direction. Black arrows indicate vergence. The colors indicate the modeled lithologies: coarse sand (red), fine sand (green), silt (blue) and clay (black). The figures have a vertical exaggeration of 4.

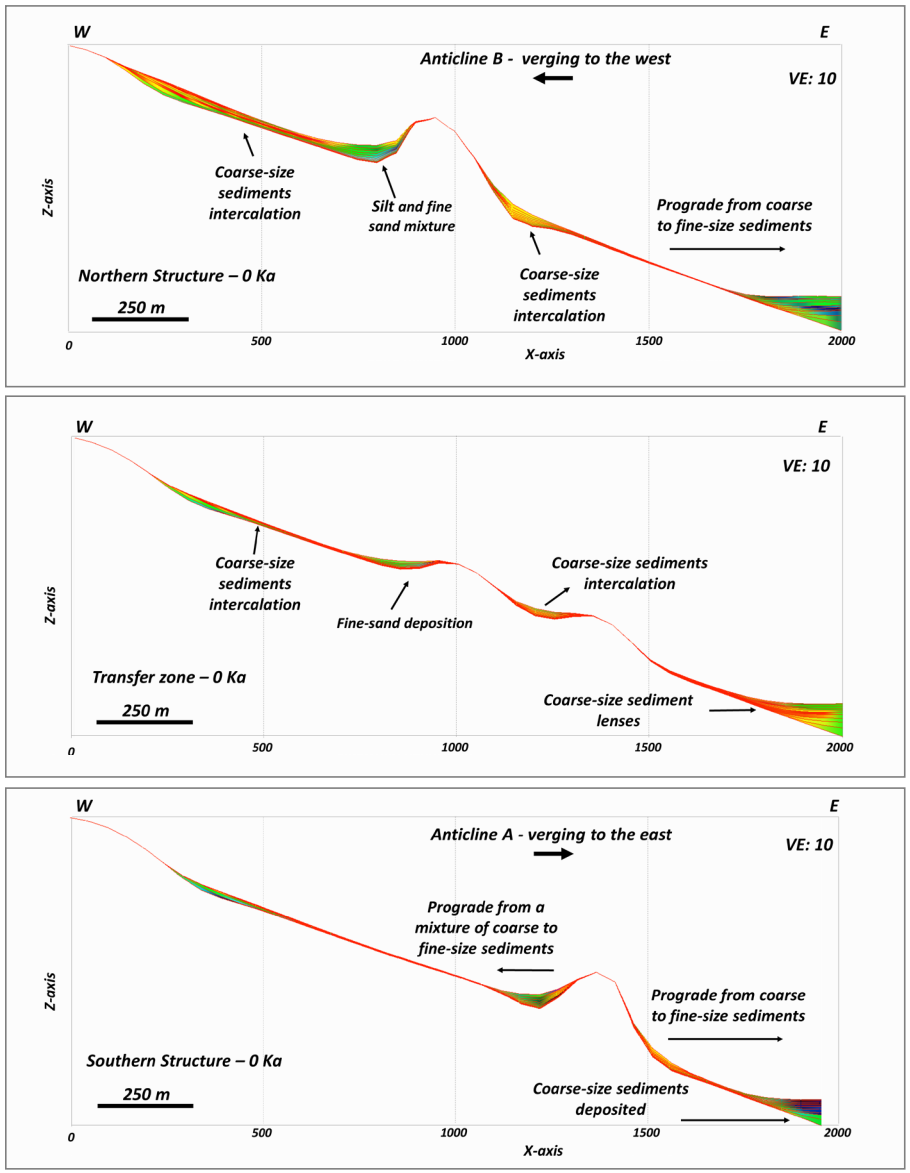

Figure 27. Cross-sections through the modeled area showing the sediment distribution pattern from west to east at the end of the simulation. Cross-section through the northern anticline. B. Cross-section north of the transfer zone. C. Cross-section through the southern anticline. The colors indicate the modeled lithologies: coarse sand (red), fine sand (green), silt (blue) and clay (black). Cross-sections have a vertical exaggeration of 10.

The cross-section through the southern structure (Figure 27C) shows the same sediment distribution pattern than in the northern structure. Towards the west, the sediments prograde from the backlimb from coarse-size sediments to a mix of fine sediments with a little amount of fine sand. Towards the east, the sediments prograde from the forelimb from coarse-size sediments (from red to green colors) to fine-size sediments (from blue to black colors). The main difference here is the occurrence of sandy lenses (green color) at the base and the increase of the silt fraction (blue color) at the top.

4.5 Thrusts with different propagation to fault slip ratio (P/S)

This case models two listric thrusts with different propagation to fault slip ratio (P/S). The southern thrust has a higher P/S of 4, while the northern thrust has a lower P/S of 2.5. The P/S ratio controls the degree of folding, less P/S yields more folding (Hardy and Ford, 1997). For that reason, with higher P/S in the southern (east-vergent) anticline, the amount of folding decreases and the resulting structure is a wide anticline with a narrow deformation zone (Hardy and Ford, 1997). Contrary, when the P/S ratio is lower as in the northern (west-vergent) anticline, the resulting structure is a tight anticline with a steep forelimb and a wider and deeper deformation zone (Figure 28, Hardy and Ford, 1997).

This model has the same dimensions, number of cells, cell size and center of curvature for both thrust than case 2 (section 4.2). The initial surface is located 40 m below the sea-level and dips 2° towards the east. The display interval is the same from cases one to six. The source of the flow is located at the WSW boundary.

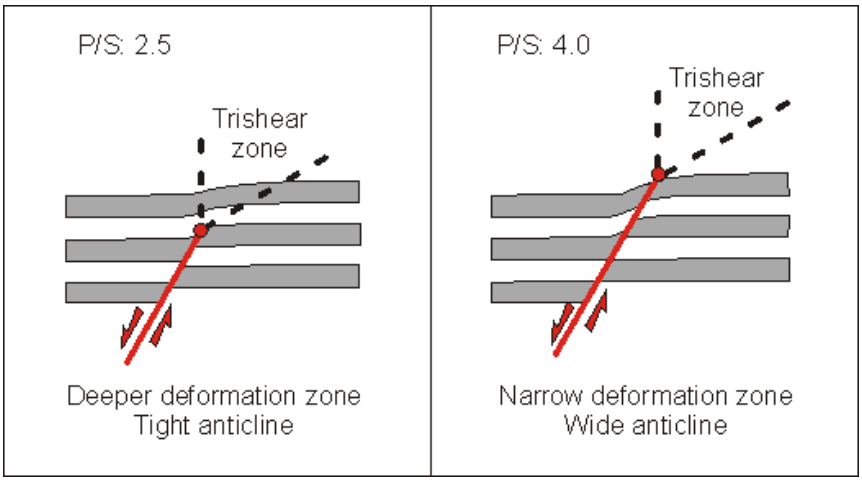

Figure 28. Schematic illustration of the trishear model for different propagation to slip ratio (P/S) values. Left, P/S 2.5 (northern thrust). Right, P/S 4.0 (southern thrust).

The initially unconfined flow is slightly to moderately disturbed by the anticlines at 70 ka (Figure 29A). At this time, the sediments eroded from the western boundary have already reached the structures where the silt and clay lithologies are trapped. Diffusion operates on both structures. Coarse-size sediments (from red to green colors) are eroded from the southern anticlinal forelimb and from the northern anticlinal backlimb. The flow carries mainly coarse-size sediments, but it is mixed with little amounts of fine-size sediments. At 40 ka (Figure 29B), the flow is totally modified and confined by both structures. The flow interacts with both structures, but it erodes more the northern structure reducing considerably its size. At this time, the flow carries mainly coarse-size sediments but, the amount of fine-size sediments is larger than at 70 ka. Towards the eastern boundary (unconfined flow area), a relatively well-defined fan geometry is observed. Two distributary channels that carry coarse-size sediments are distinguished. At 20 ka (Figure 29C), the flow is mainly disturbed by the southern structure. The northern structure (west-vergent) is not capable to deflect the flow such that the flow overpasses the structure with little disturbance. In the unconfined part of the flow system (western boundary), the flow path migrates towards the south. At this

time, one well-defined channel is observed, which carries mainly coarse-size sediments. At the end of the simulation (0 ka, Figure 29D), the northern structure modifies again the flow. One part of the flow still reaches the eastern boundary and is composed mainly of mixed fine-size sediments with little amounts of coarse-size sediments. The other part of the flow is blocked by the northern structure, which modifies its path. The flow is now totally diverted towards the northern boundary of the model. Coarse-size sediments against the northern structure are deposited. Fine-size sediments are deposited as well against the northern structure, but further towards the north.

The cross-section through the northern structure (Figure 30A) shows the same sediment deposition patterns observed in the other cases. Towards the west, a mixture of coarse-size sediments are deposited. The coarse-size sediments, as in the previous cases, consist of intercalation of fine sand (green), coarse sand (red) and the mixture of them (mainly yellow color). The sediments filling the syncline adjacent to the forelimb are mainly a mixture of fine-size sediments with a predominance of silt (from green to black color). Towards the east in the backlimb, there are less coarse sediments but still with a predominance of fine sand (green) and silt (blue). In the eastern boundary, a stack profile shows the predominance of fine sand (green) and silt (blue) mixtures from base to top. Nevertheless, a thin layer of silt at the top of the stack profile is observed.

The cross-section through the transfer zone (Figure 30B) shows a uniform vertical sediment distribution pattern from west to east, a predominance of fine sand at the base and coarse sand mainly at the top of the section. Nevertheless, the coarse sand (red color) thickness is variable and depends on the proximity of the sediment source. Between 900 – 1300 m, the coarse sand (red color) deposition is still influenced by the growth of both structures. In this zone, diffusion continues eroding and depositing coarse-size sediments near the sources and

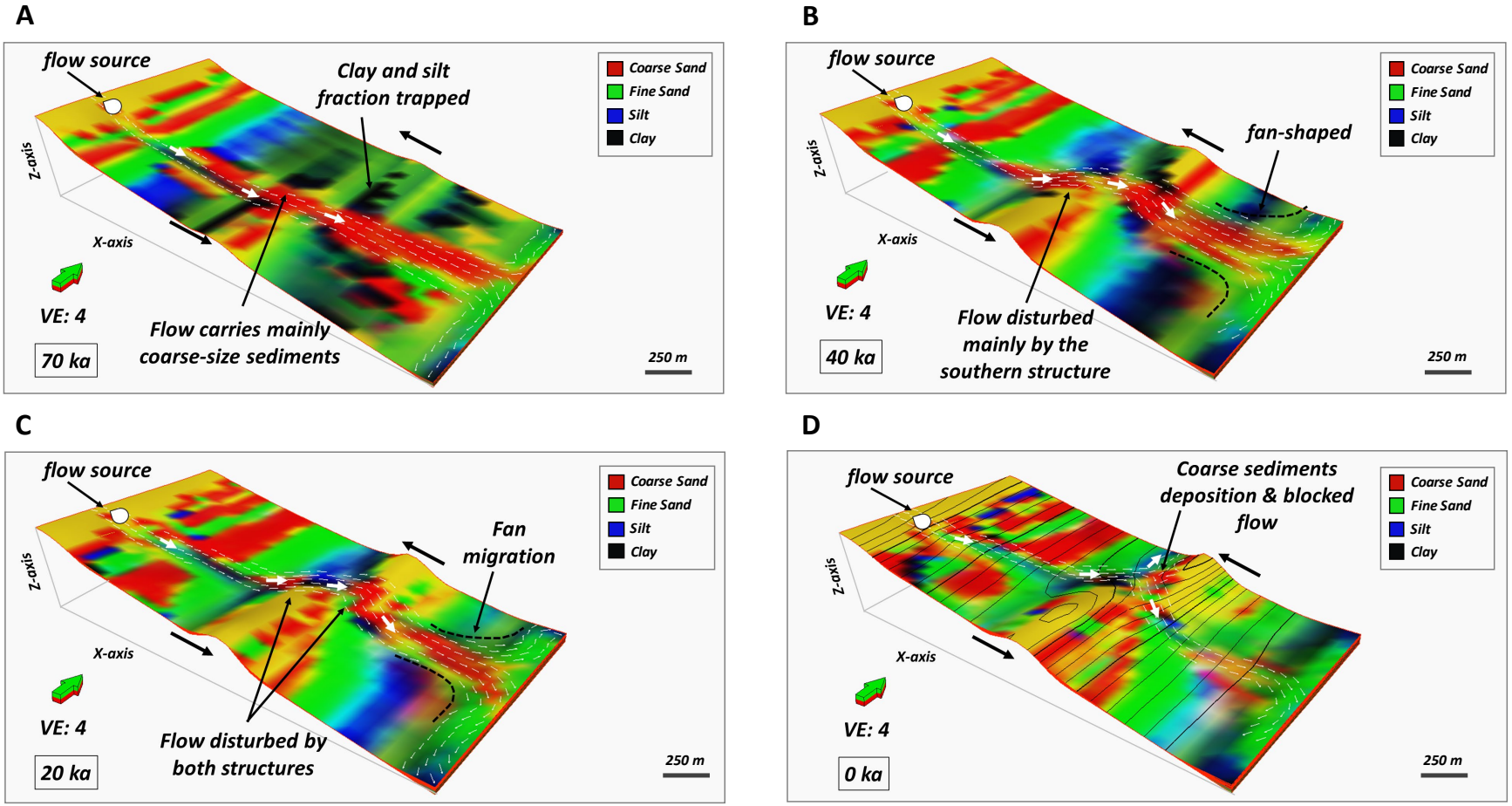

Figure 29. Case 5 – Different propagation to fault slip ratio (P/S). A, B, C, and D show the flow path and the sediment distribution pattern at 70 ka, 40 ka, 20 ka, and 0 ka, respectively. Green arrows point north. White arrows indicate the flow direction. Black arrows indicate the anticlines' vergence. The colors indicate the modeled lithologies: coarse sand (red), fine sand (green), silt (blue) and clay (black). The figures have a vertical exaggeration of 4.

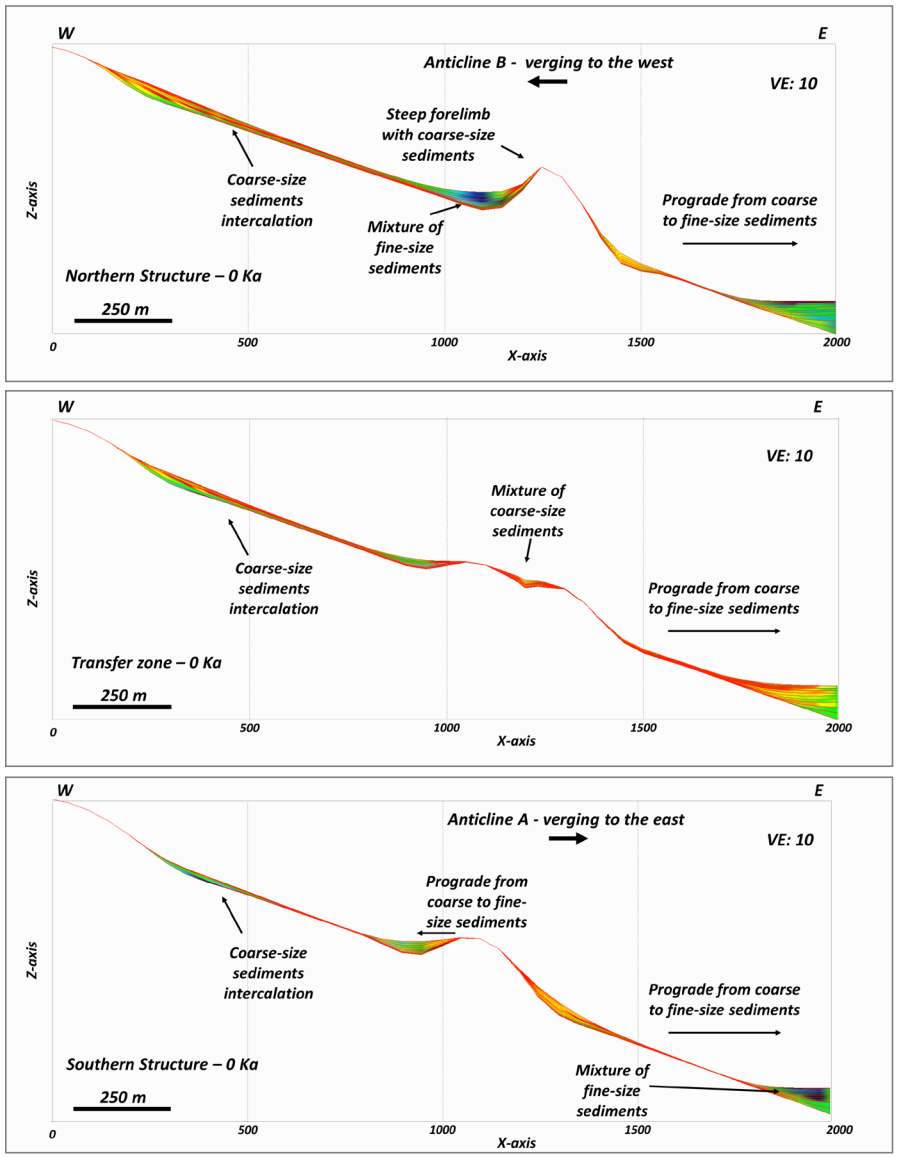

Figure 30. Cross-sections through the modeled area showing the sediment distribution pattern from west to east at the end of the simulation with thrusts of different P/S. A. Cross-section through the northern, lower P/S structure. B. Cross-section north of the transfer zone. C. Cross-section through the southern, higher P/S structure. The colors indicate the modeled lithologies: Coarse sand (red), fine sand (green), silt (blue) and clay (black). Cross-sections have a vertical exaggeration of 10.

less coarse sediments (mainly fine sand, green color) far from them.

The cross-section through the southern structure (Figure 30C), towards the east shows similar sediment distribution pattern than the northern structure. The sediments prograde from coarse-size sediments to fine-size sediments. Compared with the northern and transfer zone cross-sections, in the eastern boundary of the cross-section, a larger predominance of silt and clay (blue and black colors) is observed. Additionally, the sediments show a normally graded pattern, from coarse-size sediments at the base to fine-size sediments at the top. Towards the western part of the cross-section (between 0 – 1000 m), fine sand with little amounts of silt and clay at the base and coarse and fine sand at the top are distinguished.

4.6 Sea-level rise and thrusts with different trishear angle

This case explores different northern and southern trishear zones, besides sea-level rise during the simulation. Two listric thrusts with different trishear angle (TA) are modeled. The southern thrust has a TA of 60°, and the northern thrust has a TA of 40°. The sea-level rises 30 m. The other parameters remain similar to the base model in section 4.1. Here, the model is based on an initial surface located 70 m below sea-level (30 m) and dipping 2° towards the east. This model has the same dimensions, number of cells, cell size and display interval than the base model (section 4.1).

For both the east-vergent and west-vergent anticlines, the model generates at the backlimb of the fold, a thin but sharp syn-growth sedimentary wedge, similar to case 3 (section 4.3). In contrast to the backlimb, in the forelimb of the anticlines, a relatively gentle to moderate slope is generated with thin syn-growth strata in the southern (east-vergent) structure (Figures 31D, 32A and 32C).

Changes in sea-level have a big influence on the diffusion process when the initial surface is at shallow depths or above sea level, where erosion is strong enough to modify the thickness of the sequences (Tetzlaff, 2007). But, for this case and based on section 3.2.3, we don't expect major changes in the sediment distribution pattern since the initial surface is located 70 m below sea-level. On the other hand, the unsteady flow process is not expected to show significant changes in the sediment distribution pattern because in the current GPM version, unsteady flow is not directly influenced by these changes (Schlumberger, 2017).

The unconfined flow from the earliest cycles (100 – 70 ka, Figure 31A) deposits patches of mainly mixed sediments towards the SE. The sediment varies from coarse sand (red color) to silt (blue color). At 60 ka (Figure 31B), the flow decreases in size and migrates towards the NE. The flow pathway leaves mainly mixed sandy and silty patches towards the SE. Erosion and sediment deposition due to diffusion is observed but with low intensity. Diffusion just acts on the western boundary and the eroded sediments only reach the southern (east-vergent) structure, which traps silt and clay sediments. The flow carries and distributes the eroded sediments toward the eastern boundary with minor disturbances of the flow path due to the growing anticlines. At 40 ka (Figure 31C), diffusion-related erosion on the structures are almost non-existent. Just small coarse sand patches (red color) at the forelimb of the southern structure and the backlimb of the northern structure. To the contrary, the flow erodes and transports mainly coarse sediments toward the eastern boundary. At this time, the southern structure greatly deflects the flow. Notice that the flow decreases in size again and continue its travel towards the NE corner. At the end of the simulation (0 ka, Figure 31D), the interaction between the flow and the northern structure is bigger than at earlier times. The flow hits the northern structure and modifies its forelimb, and the anticline develops a tight shape. Now, the structure is capable of deflecting and block the flow path. Two flow paths,

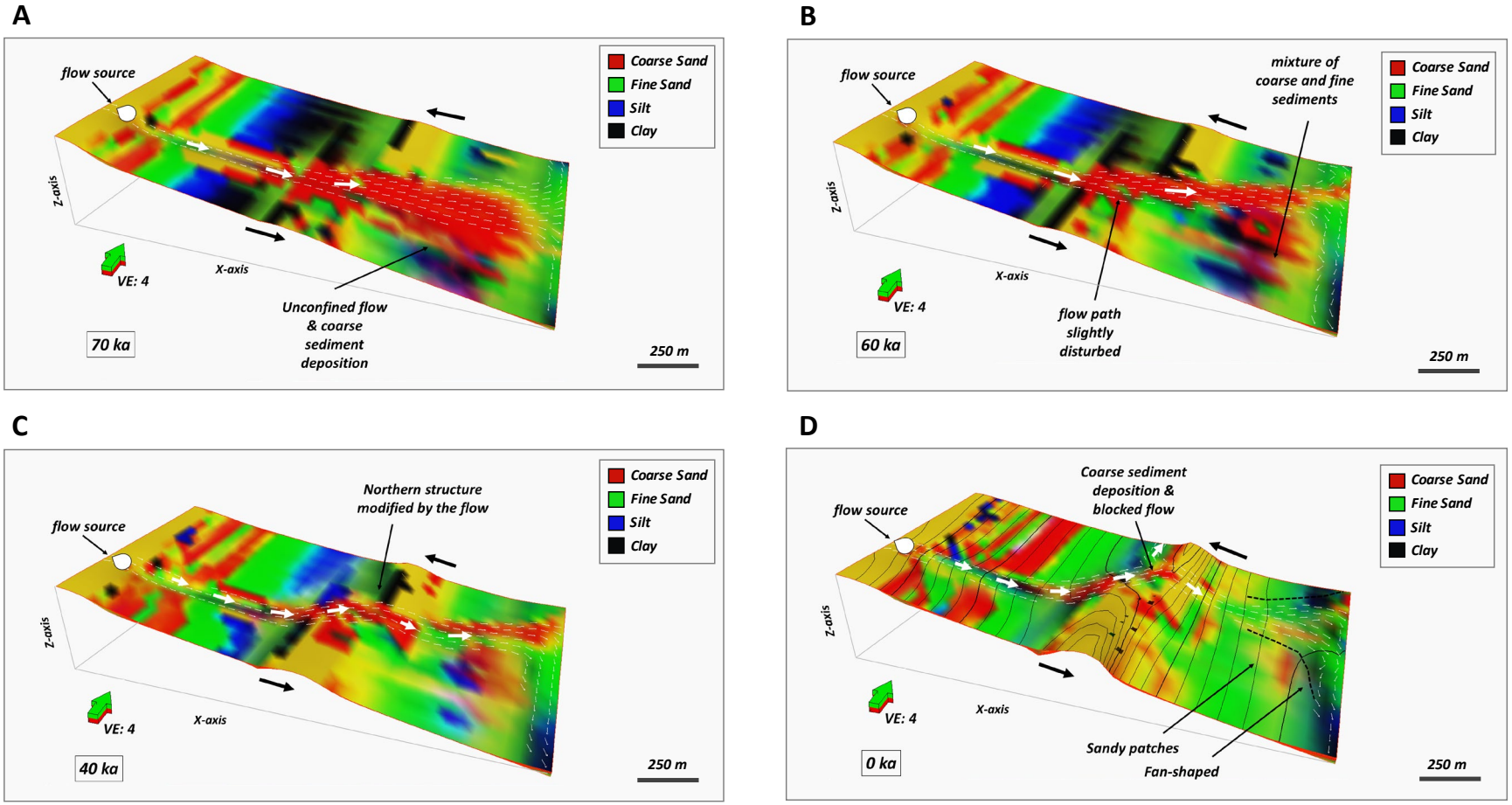

Figure 31. Case 6 – Sea-level rise. A, B, C, and D show the flow path and the sediment distribution at 70 ka, 60 ka, 40 ka, and 0 ka, respectively. Green arrows point north. White arrows indicate the flow direction. Black arrows show the anticlines' vergence. The colors indicate the modeled lithologies: coarse sand (red), fine sand (green), silt (blue) and clay (black). The figures have a vertical exaggeration of 4.

one heading toward the eastern boundary and other heading towards the north boundary, are recognized. The flow path towards the north hits the northern structure and coarse-size sediments against its forelimb are deposited. Towards the eastern boundary, the flow decreases its capacity of transport coarse sand sediments. A fan geometry composed of mainly fine sand (green color) is observed.

Towards the west in the cross-section through the northern structure (Figure 32A), intercalation of coarse sand (red color) and fine sand (green color) sediments show an increase in thickness towards the western boundary. From base to top, the syncline adjacent to the forelimb consists mainly of a mixture of fine sand (green color) and silt (blue color). In the forelimb of the anticline, coarse-size sediments are deposited. Towards the east between 1250 – 1600 m, coarse sand sediments mixed with little amounts of fine sand sediments are deposited. While between 1600 – 2000 m the predominance of fine sand (green color) with a little amount of silt (blue color) is observed. In general, coarse-size sediments near the backlimb of the anticline and fine-size sediments far from it toward the eastern boundary of the model are observed.

The cross-section north of the transfer zone (Figure 32B) shows a uniform vertical sediment distribution pattern from west to east. Here, fine sand (green color) at the base and coarse sand (red color) at the top of the section predominates. At the eastern boundary, amalgamated coarse sand fan lobes are distinguished. Nevertheless, at the top of these amalgamated fan lobes, the sediment-size diminishes, and fine sand is observed.

In the cross-section through the southern structure (Figure 32C), the sediment distribution is quite like the one observed for the northern structure. In general, at the western boundary, intercalation of coarse sand and fine sand is distinguished. In the backlimb of this anticline and the syncline next to the forelimb (between 900 – 1100 m), coarse-size sediments that

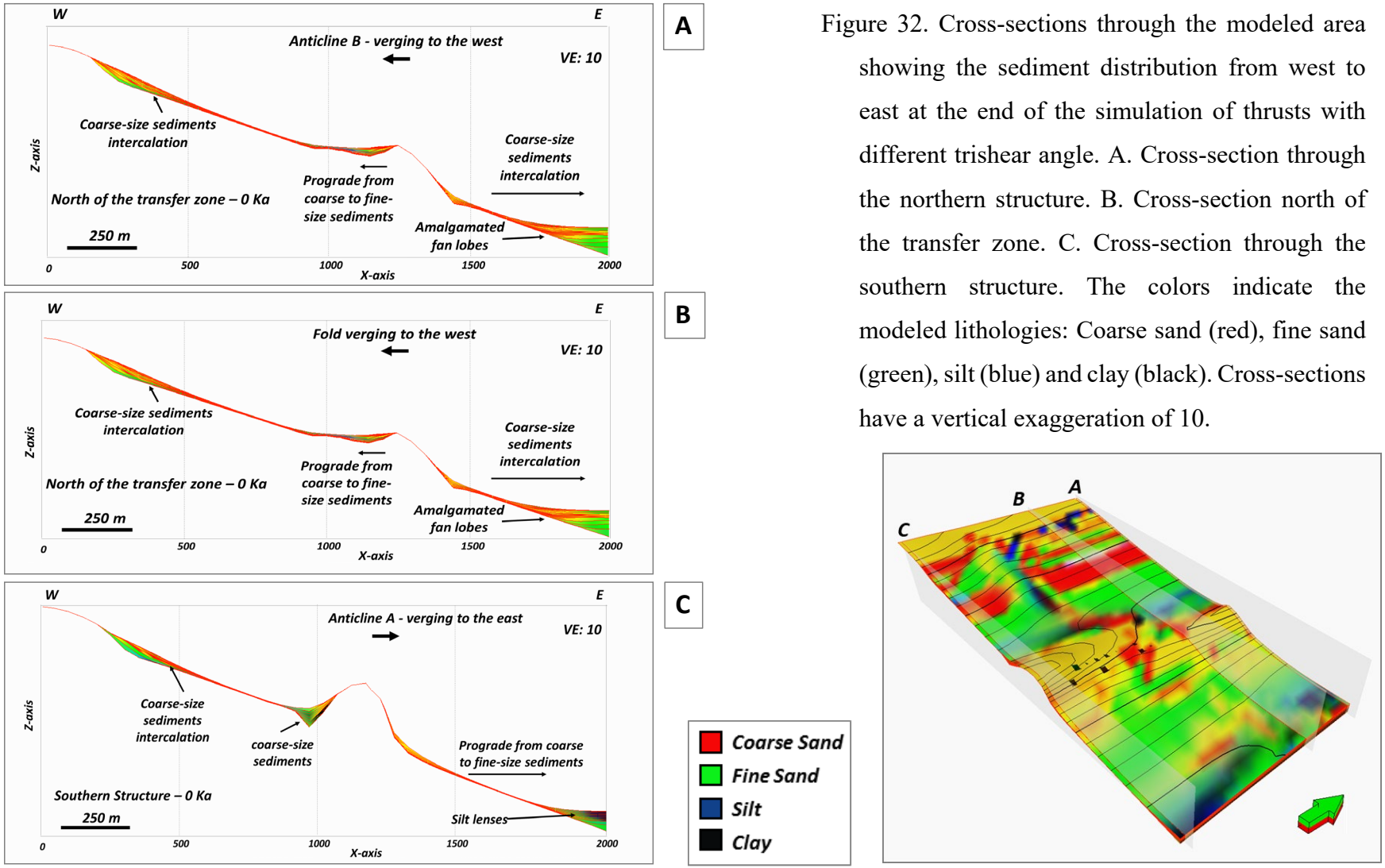

Figure 32. Cross-sections through the modeled area showing the sediment distribution from west to east at the end of the simulation of thrusts with different trishear angle. A. Cross-section through the northern structure. B. Cross-section north of the transfer zone. C. Cross-section through the southern structure. The colors indicate the modeled lithologies: Coarse sand (red), fine sand (green), silt (blue) and clay (black). Cross-sections have a vertical exaggeration of 10.

prograde towards the west from coarse sand to fine sand are deposited. Towards the east (between 1100 – 2000 m), sediments prograde from coarse to fine-size sediments. In the eastern boundary towards the top, silt lenses are deposited.

4.7 Decreasing timesteps

This case explores the effects of reducing the time steps from 10 ky to 2 ky. The total time is 100 ky, for a total of 50 simulated horizons. In order to realize a comparison with the base model or Case 1(section 4.1), this simulation has the same trishear parameters, dimensions, number of cells, cell size and initial surface elevation (-20 m).

At the start of the simulation similar to the base model in section 4.1, the eroded sediments come mainly from the top of the slope (western edge or shallower area). As expected, the coarse-size sediments (from red to green colors) are located closer to the slope, while the fine-size sediments (from blue to black colors), travel farther east. Towards the SW, sediment transport depends on both diffusion and unsteady flow. For this sector, sediment distribution depends more on the flow path. Since the flow is strong enough, it can carry coarse sediments to areas further east and a marked coarse sand path is distinguished from west to east. Here, the main difference with the base model in section 4.1 is that at this time (80 Ka), the flow is not deviated towards the north by the southern structure.

It is not until 70 ka (Figure 33A) that the flow starts to be deflected towards the north by the southern anticline. At 70 ka, for the base model in section 4.1 (Figure 33B) the flow starts to interact with both, northern and southern, anticlines. For the lower time step (current case), this interaction is not as clear. The same sediment distribution pattern is observed towards the north (diffusion dependent side), coarse-size sediments (red to green colors) near the slope and fine-size sediments (blue to black) farther east. Here, the clay fraction (black color)

has traveled long enough to reach the northern structure. In the base model (section 4.1) the structure trapped the clay fraction, but in the lower time step model this fraction overpasses the anticline. The sediment distribution towards the south is still controlled by the unsteady flow. At 40 ka (Figure 33C), the flow interacts weakly with both structures and the growth of the anticlines modifies its path. Nevertheless, the flow carries and erodes enough sediments from the northern and southern structures to create a highly mixed sediment distribution pattern. After overpassing the anticlines, the turbidity current spread sediments over the eastern area. A well-defined fan with two distributary channels that carry mainly mixed lithologies is observed. At the end of the simulation (0 ka, Figure 33E), the flow is interacting with both structures and is totally confined. The flow is deflected and confined for the northern and southern structures between the transfer zone. When the transfer zone is overpassed the flow behave as unconfined and a fan is deposited. In general, in this simulation as for the base model in section 4.1, the unsteady flow leaves patches of coarse-size sediments in their path when it migrates, while sediments that are diffused advance downhill in a linear pattern until they find a surface disturbance that impedes their travel.

Nevertheless, the most important feature here observed is, reducing the timestep has a strong effect on the grain size distribution. When compared with the base model or Case 1 (section 4.1), the sediments transported by the unsteady flow and the diffused sediments show a major proportion of mixtures. It implies that when the timestep decrease the sediments modeled have more time to be mixed (Figure 33A, 33C, 33E) instead of or remain as a single lithology (coarse sand, fine sand, silt or clay), which is the base model case (Figure 33B, 33D, 33F). The previous implies the possible characterization of the reservoir's quality with this technique is dependent of the timestep used in the simulations and, more detail analysis need to be performed.

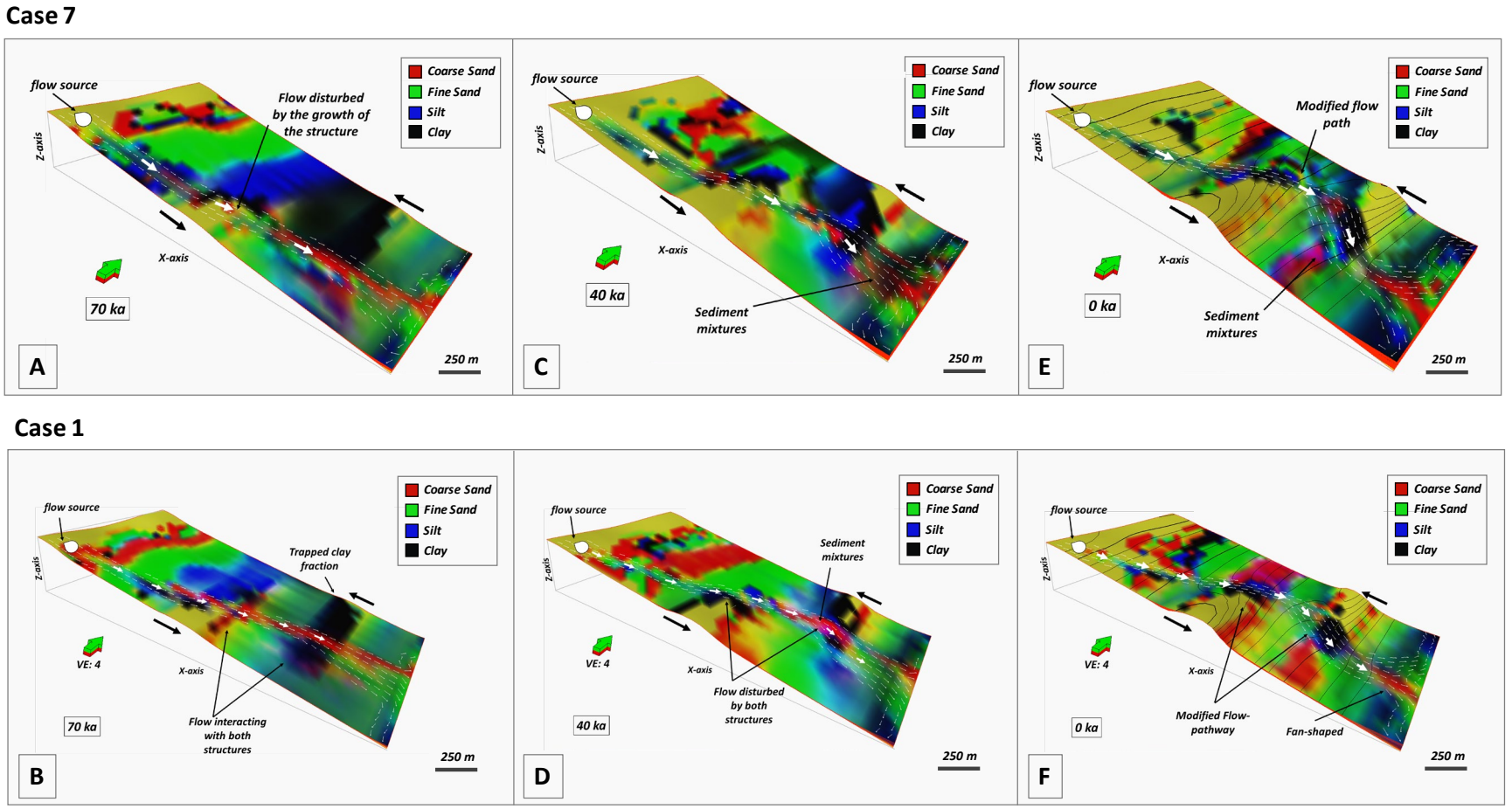

Figure 33. Case 7 – Decreasing time step. A, C, E (Case 7) and B, D, F (Case 1) show the flow path and the sediment distribution at 70 ka, 40 ka and 0 ka. Green arrows point north. White arrows indicate the flow direction. Black arrows show the anticlines' vergence. The colors indicate the modeled lithologies: coarse sand (red), fine sand (green), silt (blue) and clay (black). The figures have a vertical exaggeration of 4.

5. Discussion

This thesis tests the combination of two models, trishear and GPM, to explore turbidite sedimentation in an active tectonic setting consisting of two thrust-related, opposite verging anticlines. The results obtained help explain at geologic time scales how the interaction between tectonic deformation and sedimentation can modify the evolution of a deep water turbidite system. The trishear model used in this thesis can simulate thrust-related anticlines decreasing in fault slip along strike and with opposite vergence, while GPM models geological processes such as unsteady flow and diffusion. Because both models consider time variations, it is possible to understand how active tectonic deformation modifies sediment distribution and how the presence of growing structures affect the channel pathways.

The results are based in seven cases that model two thrust-related anticlines (northern and southern structures) that switch vergence along the strike. In the first four cases, the structures evolve from gently dipping to steeply dipping with constant trishear angle (TA) and fault propagation to slip ratio (P/S). In cases 5 and 6, more intensive deformation was applied to the structures and the trishear angle (TA) and propagation to slip ratio (P/S) was set different for each thrust. And Case 7 shows the main sediment distribution pattern differences when the timestep is decreased from 10 ky to 2 ky. The comparison is realized with the base model (Case 1, section 4.1). In all cases, the progressive evolution of the anticlines result in syn-growth sedimentary layers folded over the structures that experience significant thinning onto the crest of the anticlines. These results suggest that the structure growing is largest over the entire simulation interval and the sedimentation cannot keep pace with the active deformation. This imbalance favors variations in channel geometry, channel pathway and, sediment distribution. Since forward modeling is used to determine the general response of

regional geological processes, the software needs to be integrated with other tools and high-resolution data (seismic data, core data, high-resolution image interpretation among others) in order to perform a proper reservoir characterization (Acevedo, et al., 2014). Forward modeling results, without the integration of high-resolution data and other reservoir characterization methods, are more of instructive quality (Acevedo, et al., 2014). For that reason, this method alone is not enough to determine channel-levee geometry changes and their responses to the active structures (internal levee reflections as downlap, progressive rotation among others). These changes will be no discussed in this thesis.

Channel pathway response

The simulations clearly show how the flow pathway is disturbed on each time cycle by the active deformation. The anticlines evolution disturbs the flow pathway since the structures grow and, cycle by cycle, the flow is deflected, blocked or both. The flow pathway is blocked just in the cases where the anticline shape is tight (e.g. low trishear angle and low P/S ratio variation) or when both anticlines link along strike. Additionally, the structures exhibit changes not just because the structure growing but because of the continuous interaction with the flow. The amount of modification that the structures experience is controlled by two factors: i) the flow source position, and ii) the angle at which the flow reaches both structures. WSW source position favors the decrease in time that takes to the flow be confined by both structures. The continuous interaction between the confined flow and the structures allow the erosion to increase follow by the smoothed and modification of the structure (if the flow is strong enough). Orthogonal flow direction allows greater and direct interaction between the flow and the limbs of the structures.

Sediment distribution from unsteady flow response

The results show that if strong enough, the flow can erode and transport sediments from the anticlines and spread them over the fan-development area on the eastern side of the model. Furthermore, as the growth of the structures increased, so does its influence on the flow migration and its direction. It impacts the sediment distribution and the resultant fan shape which can be i) cone-shape fan elongated in the flow direction and ii) symmetrical cone-shape fan perpendicular to the strike of the structures. Since the flow migrates cycle by cycle, the sediment distribution pattern leaves sandy patches along the channel pathway and therefore a defined sediment distribution is not observed. On the contrary, when the flow is blocked and deflected, the progressive shifting of the channel result in a specific sediment distribution pattern consisting of amalgamated sand-rich layers, which are deposited and trapped against the structure (Figure 34 A and B). A similar process occurs in the zone where the submarine fan system is developed. In this zone, the continuous change in the flow direction makes the channel switch constantly across the fan surface, and amalgamated sand layers are deposited (Figure 34C). Here, it is possible to recognize in some cases how the single feeder (initial input) is divided into more distributary channels that transport and deposit mainly coarse to fine-grained sand.

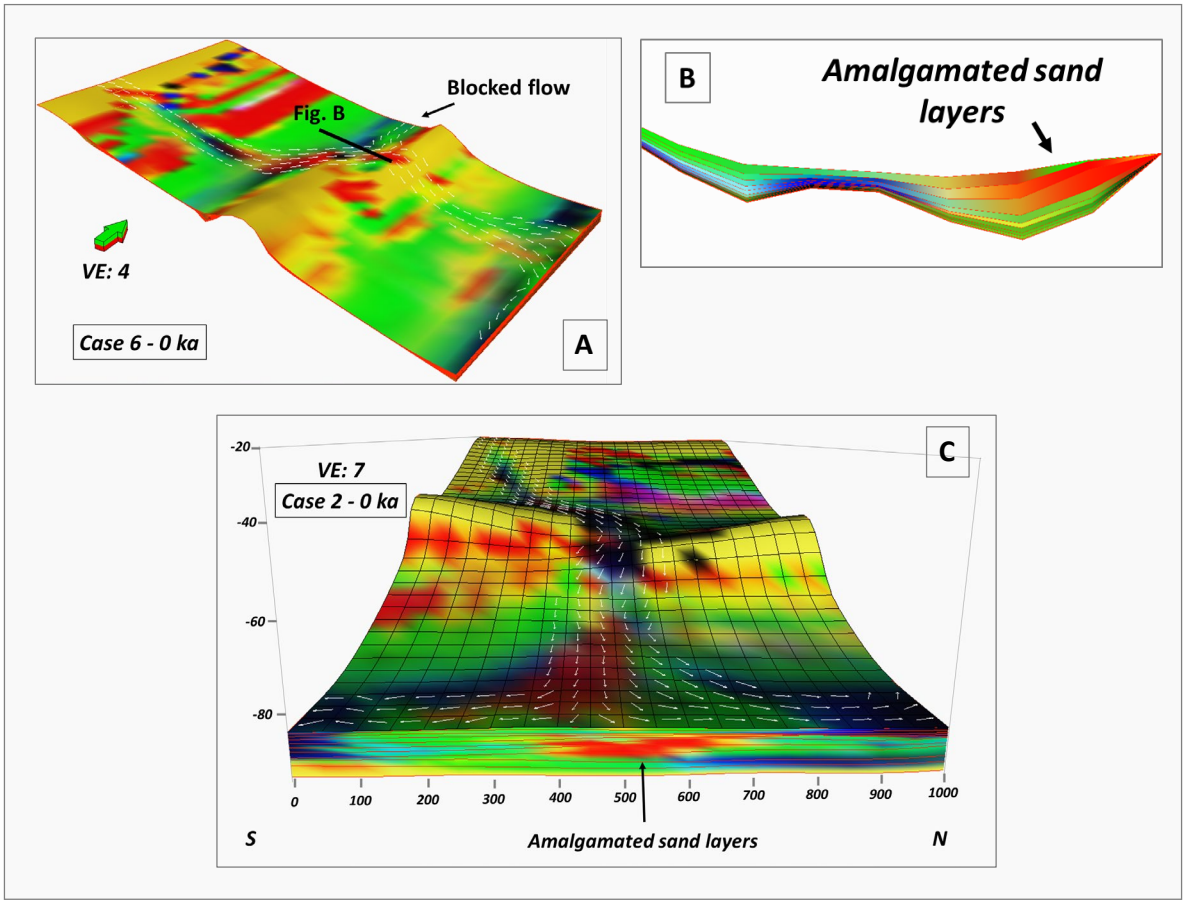

Figure 34. Amalgamated sand layers. (A) shows the flow blocked by the northern structure. (B) shows how the sand layer deposition is enhanced by the blocked flow. (C) shows the formation of amalgamated sand layers due to the constantly switching channels. Green arrow points north. The colors indicate the modeled lithologies: coarse sand (red), fine sand (green), silt (blue) and clay (black).

Sediment distribution from diffusion response

Sediment distribution due to diffusion is more uniform and has a preferential deposition pattern which is related to the location of the sediment source. In the models, the topographic highs are the main sources, which gives a total of three sources: the highest point of the initial surface, located in the western boundary and, the northern and southern anticlines. Because diffusion is a function of depth (Tetzlaff, 2007), the diffusion efficiency below sea-level

greatly decreases, but still eroded sediments are transported from the highest to the lowest topographic points. In general, the simulation results do not suggest that diffusion favors the accumulation of reservoir units adjacent to the anticlines.

Comparison with other studies

Forward modeling in this thesis proves that active deformation creates spatial and temporal variation in the channel-levee system, as suggested by Clark and Cartwright (2009), Clark and Cartwright (2011), Jolly (2014) and Grecula et al. (2017), among others. This study evidences that in zones where the sediment accumulation rate is lower than the tectonic uplift, channels largely onlap the structure until a point where the channels deflect or divert to the lateral tips of the structure as a result of the structure's growth (Jolly, 2014). Similarly, it was found that the blocking and shifting of the flow pathway increased the development of amalgamated sand-rich layers in areas adjacent to the active structure, as suggested by Clark and Cartwright (2009). Is important to notice, that the forward modeling applied in this thesis is useful to simulate geological processes. It helps to elucidate the general behavior of sedimentation coeval with tectonic deformation. Furthermore, it provides the level of resolution required to perform a predictive analysis of prospective sediments distribution. However, the lack of seismic data limits a quantitative prediction of sediments distribution as its performed by Clark and Cartwright (2009), and Jolly (2014) in terms of the relationship between the anticlines growth and the overlapping growth sequence geometries. Nevertheless, the technique and range parameters defined in this study enable to predict a qualitative sediment distribution in turbidites systems influenced by two thrust-related,

opposite verging anticlines. Although it is not a unique solution, it shows reasonable results that are validated by the conceptual model of turbidite sedimentation in these settings.

Applications

The results have important implications for the oil & gas industry because important discoveries are associated with zones of active structural deformation and deep water sedimentation (e. g. Niger delta and the Gulf of Mexico) (Jolly, 2014, Lejri et al., 2017, among others). Nevertheless, predicting the distribution of turbidite currents through time with certainty is a challenge, especially in active deformation settings (Howlett et al., 2019). The solution presented here is simple but realistic. The coupling of trishear and GPM can be used to test possible basin scenarios and for assessing geological conditions through time, by modifying a series of parameters, some of them based on analogous data (i.e. outcrops, well logs, seismic data) and other more complex and related to the model (delta time element, fluid element depth, among others). The knowledge gained here can be used to understand and even reproduce real situations, which can lead to a better understanding of reservoir distribution especially in frontier zones where the data are limited.

Forward modeling in deep-water reservoir serves to enhance the static facies modeling during the exploration stage. The 3D facies trend distributions produce by GPM, when calibrated with well-logs and seismic data, helps to improve the recognition of internal lithological channel variations. These variations can diminish the reservoir connectivity, increase the reservoir compartmentalization and greatly impact the hydrocarbon volumetric calculations.

Achieve a good matching between hard (well logs and seismic, among the others) and modeled data helps to improve and adjust the location of the sediment sources and to establish a well-defined sedimentation history. A proper match helps to clarify how much and how far the sediment where transported. Therefore, the model can be used to validate the provenience studies and recognize new possible sand-rich zones, to be tested.

The thesis indicates that the understanding of compressional environments can be improved using forward modeling. The 3D visualization of the facies stacking patterns permits, in a posterior stage, to generate stratigraphic surfaces to be used for comparison and refining of current geological interpretations of a zone. Although this is a first attempt to simulate active deformation and sedimentation, the potential of the models is promising.

6. Conclusions

This thesis uses forward modeling, coupling tectonic deformation (trishear) and sedimentation (GPM) to establish the link between deformation in deep-water thrust-related folds that switch vergence along strike, and the channel systems that interact with these structures. This can improve the prediction of potential reservoir units in these settings.

The main conclusions of the study are:

- Actively growing thrust-related anticlines that switch vergence along strike cause deflection and blocking of the channels pathways.
- The channels modify constantly its direction and shift towards low relief points. If the structure is high enough, the channel flow is blocked, and its pathway is drastically deflected toward de lateral tips of the anticlines. The transition between blocking and deflection creates sand-rich zones that are deposited against the blocking structure.
- The diffusion process is less intensive below sea-level and the sediment advances at different but mainly slow rates through time. The resulting sediment distribution consists of coarse-size sediment fractions closer to the sources and fine-sizes sediment fractions farther away.
- The development of the fan is a result of the migration and direction of the flow, which are influenced by the growth of the structures and the width of the transfer zone. When the structures are collinear (narrower transfer zone), the flow migration and direction remain relatively constant. Thus, a narrow cone-shaped fan is deposited, elongated in the flow direction. On the contrary, when the structures are more

separated between them (wider transfer zone), the variation of the flow migration and direction is higher. It produces a wider cone-shaped fan.

- The resolution of the model does not appear to create drastic changes in the model results. The high-resolution model just creates smoother and better-defined boundaries between the modelled lithologies.
- Decreasing the timesteps has drastic implications in the reservoir quality (if existing). Since the sediments have more time to be mixed, instead of remaining as a single lithology (like for display interval 10 ky) a more heterogeneous reservoir (if existing) is created. Therefore, a large impact in the hydrocarbon volumetric calculation can be obtained because of a possible reduction in the petrophysical properties quality.
- The use of both models, trishear and GPM, has several advantages since allows to simulate unsteady flows in active deformation zones with relative high accuracy. It permits to assess the different responses the flow pathway develops in these setting through the variations of parameters (geological or related to the model). It allows simulating turbidity currents in different scales. And it provides a scale-dependent detail insight of the sediment distribution patterns develops by the interaction between the turbidite currents and the active topography.
- The current simulation of thrust-related folds that switch vergence along the strike shows, the software can be adapted to any wanted experimental setup with the possibility of using a wide range of parameters that can be varied until getting the desired conditions. Several geological processes and mechanisms (unsteady flow, steady flow, compaction, tectonics among others) can be simulated and adapted to

reproduce a variety of environments with high accuracy in order to perform more suitable reservoir simulations (Schlumberger, 2016).

7. References

Abdou, M., 2001, Moving beyong prediction to Control. Free surface, turbulence, and Magnetohydrodynamics: Interactions and effects on flow control and interfacial transport.: Seminar on Science in Fusion's Enabling R&D Program.

Acevedo, A., H. A. Madhoo, A. Khramtsov, L. Noomee, and D. M. Tetzlaff, 2014, Techniques to Understand Reservoirs Associated with Deepwater Sedimentological Processes, from Basin to Field Scale - A Case Study: International Petroleum Technology Conference, p. 2-8.

Allmendinger, R. W., 1998, Inverse and forward numerical modelig of trishear fault propagation folds: Tectonics, v. 17, p. 640-656.

Cardozo, N., 2008, Trishear in 3D: Algorithms, implementation, and limitations: Journal of Structural Geology, v. 30, p. 327-340.

Cardozo, N., and S. Aanonsen, 2009, Optimized trishear inverse modeling: Journal of Structural Geology, v. 31, p. 546-560.

Cardozo, N., and J. P. Brandenburg, 2014, Kinematic modeling of folding above listric propagating thrust: Journal of Structural Geology, v. 60, p. 1-12.

Cardozo, N., and C. A.-L. Jackson, 2011, Determining the uniqueness of best-fit trishear models: Journal of Structural Geology, v. 33, p. 1063-1078.

Carter, R. M., 1998, Two models: global sea-level change and sequence stratigraphic architecture: Sedimentary Geology, v. 122, p. 23–36.

Christ, A., O. Schenk, and P. Salomonsen, 2016, Using Stratigraphic Forward Modeling to Model the Brookian Sequence of the Alaska North Slope, in N. J. Raju, ed.,

Geostatistical and Geospatial Approaches for the Characterization of Natural Resources in the Environment: New Delhi, Springer.

Clark, I. R., 2013, Interactions between sedimentation and deformation in deepwater fold and thrust belts: Ann Arbor, Michigan, USA, ProQuest LLC.

Clark, I. R., and J. A. Cartwright, 2009, Interactions between submarine channel systems and deformation in deepwater fold belts: Examples from the Levant Basin, Eastern Mediterranean sea: Marine and Petroleum Geology, v. 26, p. 1465–1482.

Clark, I. R., and J. A. Cartwright, 2012, A case study of three-dimensional fold and growth sequence development and the link to submarine channel-structure interactions in deep-water fold belds: Tectonics and Sedimentation: Implications for petroleum systems: AAPG Memoir, v. 100, p. 315-335.

Corredor, F., J. H. Shaw, and F. Bilotti, 2005, Structural styles in the deep-water fold and thrust belts of the Niger Delta: AAPG Bulletin, v. 89, p. 753-780.

Covault, J. A., and S. A. Graham, 2008, Turbidite Architecture in Proximal Foreland Basin-System Deep-Water Depocenters: Insights from the Cenozoic of Western Europe: Austrian Journal of Earth Sciences, v. 101, p. 36-51.

D'Errico, J. R., 2006, Model 2-d surfaces from scattered data, MATLAB.

Demyttenaere, R., J. P. Tromp, A. Ibrahim, P. Allman-Ward, and T. Meckel, 2000, Brunei Deep Water Exploration: From Sea Floor Images and Shallow Seismic Analogues to Depositional Models in a Slope Turbidite Setting, in P. Weimer, ed., Deep-Water Reservoirs of the World: Houston, Society for Sedimentary Geology, p. 304-317.

Deptuck, M. E., G. S. Steffens, M. Barton, and C. Pirmez, 2003, Architecture and evolution of upper fan channel-belts on the Niger Delta slope and in the Arabian Sea: Marine and Petroleum Geology, v. 20, p. 649-676.

Erslev, E. A., 1991, Trishear fault-propagation folding: Geology, v. 19, p. 617-620.

Gee, M. J. R., and R. L. Gawthorpe, 2006, Submarine channels controlled by salt tectonics: Examples from 3D seismic data offshore Angola: Marine and Petroleum Geology, v. 23, p. 443–458.

Gordon, G. S., 2014, Stratigraphic evolution and architectural analysis of structurally confined submarine fans: a tripartite outcrop-based study, Colorado School of Mines, Golden, Colorado.

Grecula, M., L. Clarke, A. Mayfield, K. Ong, and J. Stuart, 2017, Deep-Water Sequences in Static and Dynamic Basin Margin Accommodation: AAPG International Conference and Exhibition.

Haq, B. U., J. Hardenbol, and P. R. Vail, 1987, Chronology of fluctuatingsea levels since the Triassic (250 million years ago to present): Science, v. 235.

Hardy, S., and R. W. Allmendinger, 2011, Trishear: A review of kinematics, mechanics, and applications, in K. McClay, J. Shaw, and J. Suppe, Thrust fault-related folding: AAPG Memoir, v. 94, p. 95-119.

Hardy, S., and M. Ford, 1997, Numerical modeling of trishear fault propagation folding: Tectonics, v. 16, p. 841-854.

Heiniö, P., and R. J. Davies, 2007, Knickpoint migration in submarine channels in response to fold growth, western Niger Delta: Marine and Petroleum Geology, v. 24, p. 434-449.

Higgings, S., R. J. Davies, and B. Clarke, 2007, Antithetic fault linkages in a deep water fold and thrust belt: Journal of Structural Geology, v. 29, p. 1900-1914.

Higgins, S., B. Clarke, R. J. Davies, and J. Cartwright, 2009, Internal geometry and growth history of a thrust-related anticline in a deep water fold belt: Journal of Structural Geology, v. 31, p. 1597-1611.

Howlett, D. M., Z. Ge, W. Nemec, R. L. Gawthorpe, A. Rotevatn, and C. A.-L. Jackson, 2019, Response of unconfined turbidity curre nt to deep water fold and thrust belt topography : orthogonal incidence on solitary and segmented folds: Sedimentology. Accepted Author Manuscript.

Hsieh, C.-Y., K.-M. Yang, and B.-I. Chung, 2012, Trishear model and kinematics of a fault-related structure in the frontal part of Fault-and-thrust belt, NW Taiwan, National Cheng Kung University, Tainan, Taiwan.

Jolly, B. A., 2014, Channel systems and growing thrusts and folds, toe-thrust region of the deepwater Niger Delta, Imperial College London, London, England.

Kameda, A., 2000, Fault propagation folds: an assessment of kinematic (trishear) and mechanical models: Stanford Rock Fracture Project, v. 11, p. 1-17.

Kyrkjebø, R., M. Hamborg, J. I. Faleide, H. Jordt, and P. Christiansson, 2000, Cenozoic tectonic subsidence from 2D depositional simulations of a regional transect in the northern North Sea basin: The Geological Society of London, v. 167, p. 273-294.

Lejri, M., H.A. Madhoo, B. Claussmann, L. Truelove, J. Tveiten, D. Tetzlaff, and P. Salomonsen, 2017, Understanding the controls on clastic sedimentation using forward stratigraphic modeling and seismic sequence stratigraphy, AAPG SEG International conference & exhibition - ExCel, London.

Malde, P. K., 2017, Coupling of trishear fault-propagation folding and ground process modelling, University of Stavanger, Stavanger, Norway.

Medwedeff, D. A., and J. Suppe, 1997, Multibend fault-bend folding: Journal of Structural Geology, v. 19, p. 279-292.

Mitra, S., 2002, Structural models of faulted detachment folds: AAPG Bulletin, v. 86, p. 1673-1694.

Owoyemi, A. O., 2004, Sequence stratigraphy of Niger Delta, Delta field, offshore Nigeria, Texas A&M University, Texas, USA.

Pei, Y., D. A. Paton, and R. J. Knipe, 2014, Defining a 3-dimensional trishear parameter space to understand the temporal evolution of fault propagation folds: Journal of Structural Geology, v. 66, p. 284-297.

Posamentier, H. W., 2003, Depositional elements associated with a basin floor channel-levee system:case study from the Gulf of Mexico: Marine and Petroleum Geology, v. 20, p. 677–690.

Reading, H. G., and M. Richards, 1994, Turbidite Systems in Deep-Water Basin Margins Classified by Grain Size and Feeder System: AAPG Bulletin, v. 78, p. 792–822.

Schlumberger, 2016, Petrel* 2015.4 Sedimentary Simulation and Visualization Plug-in. User guide.

Schlumberger, 2017, GPM Geological Process Modeling Software. User Guide.

Skauvold, J., and J. Eidsvik, 2018, Data assimilation for a geological process model using the ensemble Kalman filter: Basin Research, v. 30, p. 730-745.

Suppe, J., 1983, Geometry and kinematics of Fault-Bend folding: American Journal of Science, v. 283, p. 684-721.

Tetzlaff, D., J. Tveiten, P. Salomonsen, A. Christ, W. Athmer, H. G. Borgos, L. Sonneland, C. Martinez, and M. F. Raggio, 2014, Geologic Process Modeling, IX Congreso de Exploración y Desarrollo de Hidrocarburos - IAPG, Mendoza, Argentina, p. 1-16.

Tetzlaff, D. M., 2005, Modelling Coastal Sedimentation through Geologic Time: Journal of Coastal Research v. 21, p. 610-617.

Tetzlaff, D. M., 2007, Interaction among sedimentation, compaction, and groundwater flow in coastal settings: The Geological Society of London, v. 426, p. 65-87.

Zehnder, A., and R. Allmendiger, 2000, Velocity field for the trishear model: Journal of Structural Geology, v. 22, p. 1009-1014.